

OmniVGGT: Omni-Modality Driven Visual Geometry Grounded Transformer

Haosong Peng^{1*}, Hao Li^{2*}, Yalun Dai², Yushi Lan², Yihang Luo², Tianyu Qi³,
Zhengshen Zhang⁴, Yufeng Zhan^{1✉}, Junfei Zhang^{5✉}, Wenchao Xu^{1✉}, Ziwei Liu²
¹HKUST ²NTU ³SYSU ⁴NUS ⁵Alibaba Group

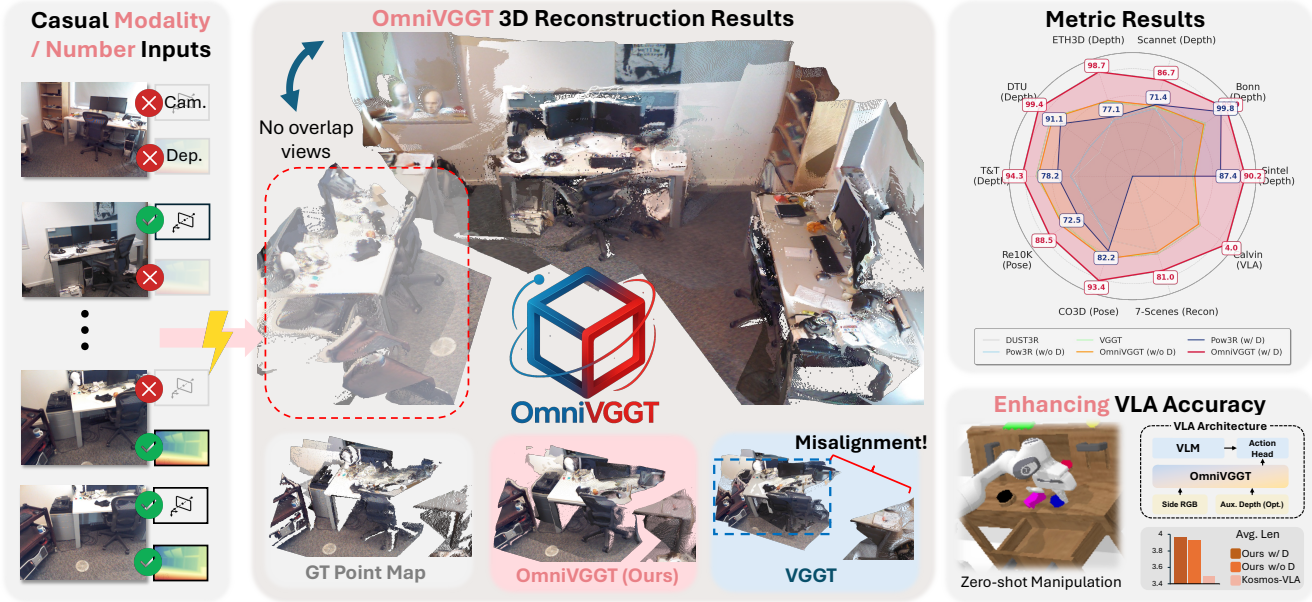


Figure 1. We proposed OmniVGGT, a spatial foundation model that can effectively benefit from an arbitrary number of auxiliary geometric modalities (depth, camera intrinsics & pose) to obtain high-quality 3D geometric results. Experimental results show that OmniVGGT achieves state-of-the-art performance across various downstream tasks and further improves performance on robot manipulation tasks.

Abstract

General 3D foundation models have started to lead the trend of unifying diverse vision tasks, yet most assume RGB-only inputs and ignore readily available geometric cues (e.g., camera intrinsics, poses, and depth maps). To address this issue, we introduce **OmniVGGT**, a novel framework that can effectively benefit from an arbitrary number of auxiliary geometric modalities during both training and inference. In our framework, a **GeoAdapter** is proposed to encode depth and camera intrinsics/extrinsics into a spatial foundation model. It employs zero-initialized convolutions to progressively inject geometric information without disrupting the foundation model’s representation space. This design ensures stable optimization with negligible overhead, maintaining inference speed comparable to VGGT even with multiple additional inputs. Addition-

ally, a **stochastic multimodal fusion** regimen is proposed, which randomly samples modality subsets per instance during training. This enables an arbitrary number of modality inputs during testing and promotes learning robust spatial representations instead of overfitting to auxiliary cues. Extensive experiments on monocular/multi-view depth estimation, multi-view stereo, and camera pose estimation demonstrate that OmniVGGT outperforms prior methods with auxiliary inputs and achieves state-of-the-art results even with RGB-only input. To further highlight its practical utility, we integrated OmniVGGT into **vision-language-action (VLA) models**. The enhanced VLA model by OmniVGGT not only outperforms the vanilla point-cloud-based baseline on mainstream benchmarks, but also effectively leverages accessible auxiliary inputs to achieve consistent gains on robotic tasks. Project Page: <https://livioni.github.io/OmniVGGT-official/>

*Equal Contribution. ✉Corresponding Authors.

1. Introduction

Similar to how large language models (LLMs, e.g., ChatGPT [2]) have revolutionized the field of NLP, building a general model for 3D perception (e.g., VGGT [63]) is emerging as a new paradigm in the 3D vision community. Unlike traditional approaches that focus on solving specific tasks (e.g., monocular and stereo depth estimation [19, 31], pose estimation [3, 61], or novel view synthesis [25, 39]), recent methods [29, 63, 66] have demonstrated tremendous potential in addressing all these tasks in a unified manner using feed-forward architectures.

While these general solutions aim to establish unified representations for various 3D downstream tasks, they typically overlook efforts to *unify diverse input modalities*. Most methods [29, 63, 66] are limited to accepting only RGB images as input, neglecting the rich multimodal inputs commonly found in 3D vision, such as depth maps and camera poses. Recent Pow3R [22] has made attempts to incorporate multimodal inputs, but they are typically limited to handling at most two inputs (e.g., RGB pair and depth pair). However, in real-world 3D vision applications, an *arbitrary number* of multimodal inputs is often available. For example, virtual/augmented reality (VR/AR) utilizes RGB-D data to acquire depth maps [13, 18, 43], some autonomous driving strategies leverage LiDAR to capture point clouds [10, 28, 55], and robotic applications may incorporate knowledge of camera intrinsics and/or extrinsics (e.g., pose) [20, 24]. Therefore, the ability to *seamlessly benefit from these accessible multimodal inputs to enhance model performance* is of critical importance.

To address this problem, we propose OmniVGGT, which introduces a flexible input scheme that can benefit from an arbitrary number of various geometric modalities when available. First, we introduce a lightweight **GeoAdapter** to effectively incorporate geometric cues (depth and camera parameters). A key challenge arises from their differing properties: unlike a depth map, which provides dense, per-pixel spatial cues, the camera pose is a global attribute. Therefore, directly injecting encoded 3D camera information can destabilize the feature space of large-scale foundation models, leading to severe issues during early training. To mitigate this and preserve the foundation model’s high-quality feature representations, we employ zero convolution to process the camera pose, progressively initializing the adapter’s parameters from zero. This strategy ensures training stability and maintains the foundation model’s superior representations, with negligible added computational overhead. Our lightweight design ensures that despite multiple additional inputs, the inference speed of OmniVGGT remains comparable to that of the vanilla VGGT.

Second, powered by our **stochastic multimodal fusion strategy**, OmniVGGT can leverage arbitrary numbers of geometric modality inputs during testing, significantly en-

hancing its practicality and generality compared to vanilla VGGT and Pow3R. Notably, this stochastic strategy enables the model to learn more generalized and robust 3D spatial representations from diverse auxiliary modalities, rather than merely fitting the additional 3D information.

Extensive experiments on various 3D vision tasks (e.g., mono-/multi-view depth estimation, multi-view stereo, and camera pose estimation) demonstrate that our method not only significantly outperforms existing approaches when auxiliary modality inputs are available but also surpasses state-of-the-art methods when using RGB-only inputs. Moreover, to thoroughly validate the practical value of our model, we integrate OmniVGGT with vision-language-action (VLA) models and conduct extensive robotic manipulation experiments. Evaluations show that the enhanced VLA model exhibits superior spatial understanding capabilities compared to the vanilla point-cloud-based baseline, while simultaneously demonstrating its capacity to exploit accessible auxiliary inputs (e.g., depth) for consistent gains on robotic tasks.

2. Related Work

2.1. 3D Reconstruction

Traditional methods [11, 21, 70, 71] employed a Structure-from-Motion (SfM) framework to ascertain camera positions and produce sparse point clouds. Recently, advancements such as Neural Radiance Fields (NeRF) [39] and 3D Gaussian Splatting (3DGS) [25] have become ubiquitous in 3D vision thanks to their photo-realistic characteristics and superior novel-view synthesis capabilities, enabling applications from enhancing immersive environments in VR/AR and improving spatial awareness in robotics, to supporting urban planning and cultural heritage digitization [5, 14, 15, 59]. However, these methods typically require per-scene optimization and accurate camera poses as input, which limits their generalization and scalability.

2.2. Spatial Foundation Model

More recently, advancements in deep learning have introduced novel alternatives to traditional SfM methods. DUST3R [66] represents a significant deviation from conventional SfM pipelines by predicting point clouds from image pairs without relying on geometric constraints or inductive biases. Building on this paradigm, several works have proposed variations with distinct architectural innovations. MAST3R [29] improves the estimation of the pixel-wise correspondence between image pairs, strengthening the efficacy of unconstrained feed-forward models for SfM tasks. CUT3R [65] introduces a recurrent formulation of DUST3R, achieving computational efficiency at the expense of marginal accuracy degradation. More recently, VGGT [63] proposes a multi-view architecture that

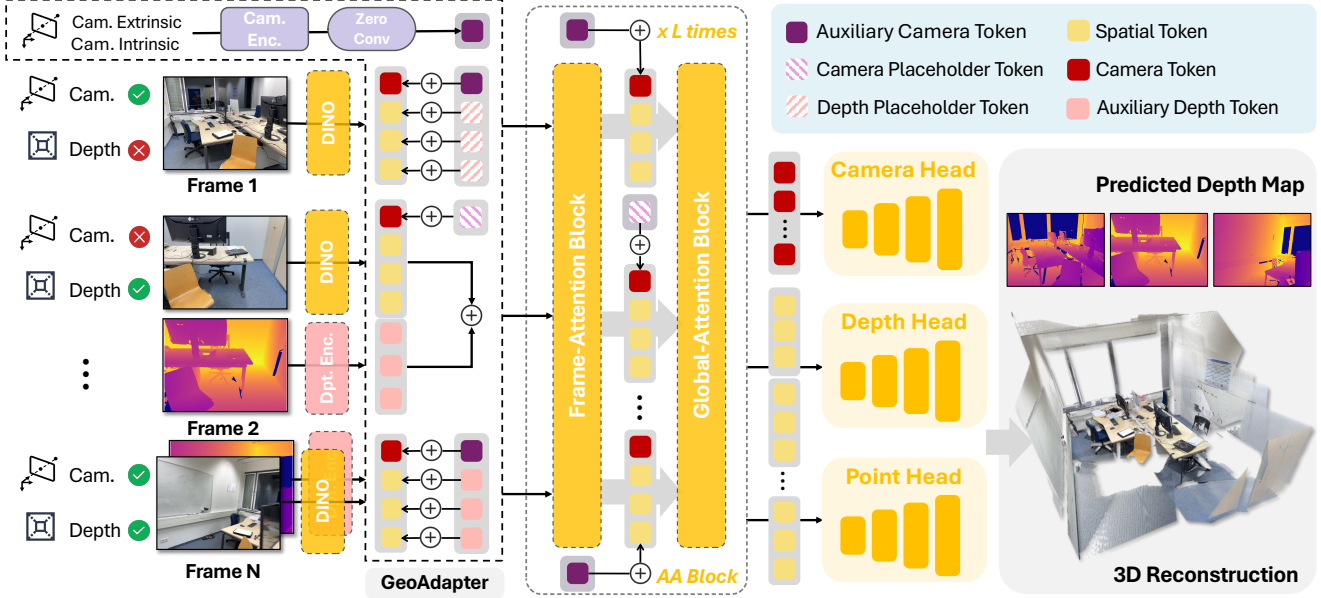


Figure 2. **Overview of OmniVGGT.** OmniVGGT takes as input a set of images together with an arbitrary number of corresponding camera parameters (poses and intrinsics) or depth maps. Camera placeholder tokens and depth placeholder tokens are used to substitute the tokens for which auxiliary information is missing. The inputs are processed through L layers of Alternating-Attention, and finally, three prediction heads are employed to output depth maps, camera poses, and 3D point maps.

processes multiple images simultaneously, moving beyond pairwise processing to improve reconstruction consistency and robustness. Owing to its strong generalization ability, it has already been applied in fields such as SLAM [36] and 4D reconstruction [27, 79], and novel view synthesis [35]. However, while these methods aim to create unified 3D representations broadly applicable to downstream tasks, they are often limited to RGB-only inputs, neglecting the substantial benefits afforded by rich auxiliary 3D modalities.

3. Preliminary

We follow the recently proposed VGGT [63] method that directly infers all key 3D attributes of a scene within seconds. The input image set \mathbf{I} is first patchified into spatial tokens \mathbf{e}_f via DINO backbone [40]. Spatial tokens from all frames are concatenated with learnable camera tokens \mathbf{e}_c and register tokens \mathbf{e}_r , and then processed jointly by the transformer encoder \mathcal{E} :

$$(\hat{\mathbf{e}}_c, \hat{\mathbf{e}}_r, \hat{\mathbf{e}}_f) = \mathcal{E}(\mathbf{e}_c, \mathbf{e}_r, \mathbf{e}_f). \quad (1)$$

VGGT adopts an Alternating-Attention (AA) scheme as its encoder, where frame-wise self-attention captures intra-image structures, and global self-attention aggregates information across views. After being processed by AA blocks (L layers in total), refined spatial tokens $\hat{\mathbf{e}}_f$ and camera tokens $\hat{\mathbf{e}}_c$ are retained for prediction, while register tokens $\hat{\mathbf{e}}_r$ are discarded. For depth and point map predictions, VGGT uses the DPT heads [45] as dense prediction heads,

and feeds the dense feature to get the depth maps $\hat{\mathbf{D}}$, 3D point maps $\hat{\mathbf{P}}$, and corresponding confidence map $\hat{\mathbf{Y}}$. For the camera head, all camera tokens are passed through four self-attention layers followed by a linear layer to predict the camera intrinsics and extrinsics.

4. Methodology

This section details OmniVGGT: 1) We articulate its core capability to leverage arbitrary auxiliary inputs in Section 4.1. 2) We introduce the GeoAdapter as our key architecture for multimodal injection in Section 4.2. 3) We discuss the stochastic training strategy pivotal for multimodal fusion Section 4.3.

4.1. Overview of OmniVGGT

As illustrated in Fig. 2, our OmniVGGT ingests an image set $\mathbf{I} = \{I_i\}_{i=1}^N$, along with an arbitrary number of auxiliary inputs such as camera parameters $\mathbf{C} = \{C_j\}_{j=1}^Q$ and depth maps $\mathbf{D} = \{D_k, M_k\}_{k=1}^O$ (where $Q \leq N, O \leq N$), to guide more accurate and robust 3D scene reconstruction. Each image $I \in \mathbb{R}^{3 \times H \times W}$ may be associated with known camera parameters $C = \{K, G\}$, i.e., intrinsics $K \in \mathbb{R}^{3 \times 3}$ and pose $G = [R | t] \in \mathbb{R}^{4 \times 4}$, or with a known depth map $D \in \mathbb{R}^{H \times W}$ accompanied by a corresponding mask $M \in \{0, 1\}^{H \times W}$ for valid depth. All images are simultaneously fed into the OmniVGGT network, which fully leverages the available camera parameters and depth maps (if provided) to produce the predicted 3D point maps along with complete

camera poses and intrinsics, depth maps, and corresponding confidence maps in an end-to-end manner.

4.2. GeoAdapter for Stochastic Multimodal Inputs

Our lightweight GeoAdapter consists of a camera adapter and a depth adapter, both of which include auxiliary geometric information normalization, encoding, and injection steps. It seamlessly incorporates prior information into the encoder, enabling more effective feature fusion.

Camera Adapter. First, given a set of camera intrinsics $\{K_j\}_{j=1}^Q$ and poses $\{G_j\}_{j=1}^Q = [R \mid t]$, we first align the coordinate system origin with the first camera. We then compute the average distance between the remaining cameras and the origin, using it as a scale factor to normalize all camera poses. The formulations are as follows:

$$s = \frac{1}{Q-1} \sum_{j=2}^Q \|t_j - t_1\|_2, \quad j = 2, \dots, Q, \quad (2)$$

$$G'_j = G_j G_1^{-1}; \quad t'_1 = \mathbf{0}; \quad t'_j = \frac{t_j - t_1}{s}; \quad j = 2, \dots, Q. \quad (3)$$

Second, the intrinsics and normalized poses are parameterized into a feature vector $\{K, G\}$ as $\mathbf{g} = \{\mathbf{q}, \mathbf{t}, \mathbf{f}\}$ follow [62], where $\mathbf{q} \in \mathbb{R}^4$ denotes the rotation quaternion, $\mathbf{t} \in \mathbb{R}^3$ denotes the translation vector, and $\mathbf{f} \in \mathbb{R}^2$ denotes the field of view. After that, \mathbf{g} is fed into a dedicated camera encoder $\mathcal{E}_l^{\text{cam}}(\cdot)$ before l -th AA block to obtain the auxiliary camera tokens $\mathbf{e}_c^{\text{aux}}$:

$$\mathbf{e}_{c,i,l}^{\text{aux}} = \mathcal{E}_l^{\text{cam}}(\mathbf{g}_j), \quad j = 0, \dots, Q, \quad l = 0, \dots, L, \quad (4)$$

For images without camera information, we use a zero vector $\mathbf{e}_c^{\text{plh}}$ as the camera placeholder token to replace the missing auxiliary camera token. Third, we pass all the auxiliary camera tokens through a zero-conv layer $\mathcal{ZC}_l(\cdot)$, and then add the processed tokens to the camera tokens:

$$\mathbf{e}'_{c,i,l} = \mathbf{e}_{c,i,l} + \mathcal{ZC}_l(m_i(\mathbf{e}_{c,i,l}^{\text{aux}}) + (1 - m_i)\mathbf{e}_c^{\text{plh}}), \quad (5)$$

where $m_i \in \{0, 1\}$ is a binary indicator that equals 1 if the image has auxiliary camera parameters and 0 otherwise.

Depth Adapter. First, auxiliary depth maps $\{D\}_{k=1}^O$ are first normalized on a per-batch basis. For each depth map $\{D_k\}_{k=1}^O$, we identify valid pixels using the corresponding mask. The valid depths are then normalized by the mean depth value computed over all valid pixels in the batch and further concatenated along the channel dimension:

$$X = [D; M], \quad X \in \mathbb{R}^{2 \times H \times W}. \quad (6)$$

Second, X is fed into a depth encoder $\mathcal{E}^{\text{dpt}}(\cdot)$ to obtain the auxiliary depth token $\mathbf{e}_d^{\text{aux}}$, which consists of a dedicated convolutional layer that tokenizes X and aligns the dimension of spatial token:

$$\mathbf{e}_{d,k}^{\text{aux}} = \mathcal{E}^{\text{dpt}}(X_k), \quad k = 0, \dots, O. \quad (7)$$

For images without reference depth information, we use a separate depth placeholder token instead. Third, the auxiliary depth token and placeholder token are then directly added to the corresponding spatial token:

$$\mathbf{e}'_{f,i} = \mathbf{e}_{f,i} + \left(n_i(\mathbf{e}_{d,i}^{\text{aux}}) + (1 - n_i)\mathbf{e}_d^{\text{plh}} \right) \quad (8)$$

where $n_i \in \{0, 1\}$ is a binary indicator that equals 1 if the image has auxiliary depth maps and 0 otherwise. Through extensive ablation study, we observe that applying an additional zero-conv layer to the depth branch is redundant, as it disrupts the effective integration of depth information.

4.3. Training Procedure

Training Objective. Following VGGT [63], our training objective is a multi-task loss comprising three components: camera, depth, and point map supervision. The total loss is defined as $\mathcal{L} = \mathcal{L}_{\text{camera}} + \mathcal{L}_{\text{depth}} + \mathcal{L}_{\text{pmap}}$. The camera loss, $\mathcal{L}_{\text{camera}}$, supervises the predicted camera parameters $\hat{\mathbf{g}}_i$ against the ground truth \mathbf{g}_i using an ℓ_1 regression loss. For the depth loss $\mathcal{L}_{\text{depth}}$ and the point map loss $\mathcal{L}_{\text{pmap}}$, we adopt the confidence-aware regression loss. Each of these is further augmented with a gradient-based term to enhance local geometric consistency.

Stochastic Multimodal Fusion Strategy. To enable the ability that accepting arbitrary input combinations at inference time, we train the network on batches of images where auxiliary information is stochastically assigned. Specifically, for an image sequence of length S , we first uniformly sample a number $Q \in [0, S]$ to determine the quantity of images to be provided with ground truth (GT) camera parameters. We then assign these camera annotations to the first Q images in the sequence. In contrast, for depth GT, a number $O \in [0, S]$ is sampled independently, and these O annotations are assigned to randomly selected indices within the sequence. This stochastic assignment strategy simplifies the training process while ensuring the model is robust to various partial-information scenarios during inference. Furthermore, to ensure stability and handle the auxiliary-free case, a subset of training batches (with probability $p\%$) is processed using only raw RGB images.

5. Experiments

Datasets. We train our model using images from 19 public datasets, including: ARKitScenes [6], Blended-MVS [71], DL3DV [33], Dynamic Replica [23], HyperSim [47], Kubric [16], MapFree [3], MegaDepth [31], Matterport 3D [44], MVS-Synth [21], ScanNet [12], ScanNet++ [72], Spring [38], TartanAir [67], UASOL [7], Unreal 4K [58], Virtual KITTI [9], Waymo [56], WildRGBD [68]. These datasets cover both synthetic and real-world content, indoor and outdoor environments, as well as

Table 1. **Impact of Auxiliary Information Injection.** We evaluate the performance of depth and pose estimation when varying the percentage of injected ground-truth information on the unseen Sintel dataset [8]. The absolute improvements over the baseline (w/o aux. information) are highlighted in green, and the best results are shown in **bold**.

Method	Aux. information (%)		Depth		Camera		
	Depth	Camera	Abs Rel↓	$\delta < 1.25 \uparrow$	RRA@5°↑	RTA@ 5°↑	AUC@30° ↑
VGGT	✗	✗	0.722	70.81	95.69	53.92	70.55
OmniVGGT	✗	✗	0.558	71.46	96.15	54.01	70.83
OmniVGGT + aux. information	30	✗	0.169 (+0.389)	78.92 (+7.46)	96.65 (+0.50)	54.15 (+0.14)	71.43 (+0.60)
	50	✗	0.150 (+0.408)	80.93 (+9.47)	96.65 (+0.50)	55.90 (+1.89)	71.49 (+0.66)
	70	✗	0.124 (+0.434)	83.24 (+11.78)	96.65 (+0.50)	56.89 (+2.88)	73.68 (+2.85)
	100	✗	0.106 (+0.452)	85.95 (+14.49)	96.93 (+0.78)	59.73 (+5.72)	77.16 (+6.33)
	✗	30	0.555(+0.003)	72.45 (+0.99)	98.56 (+2.41)	61.44 (+7.43)	75.87 (+5.04)
	✗	50	0.554 (+0.004)	72.43 (+0.97)	98.67 (+2.52)	63.76 (+9.75)	77.90 (+7.07)
	✗	70	0.554 (+0.004)	72.49 (+0.90)	98.84 (+3.82)	66.91 (+12.9)	79.72 (+8.80)
✗	100	0.553 (+0.005)	72.36 (+0.90)	99.97 (+3.82)	75.83 (+21.82)	85.35 (+14.52)	
	100	100	0.106 (+0.452)	85.95 (+14.49)	99.97 (+3.82)	76.33 (+22.32)	85.99 (+15.16)

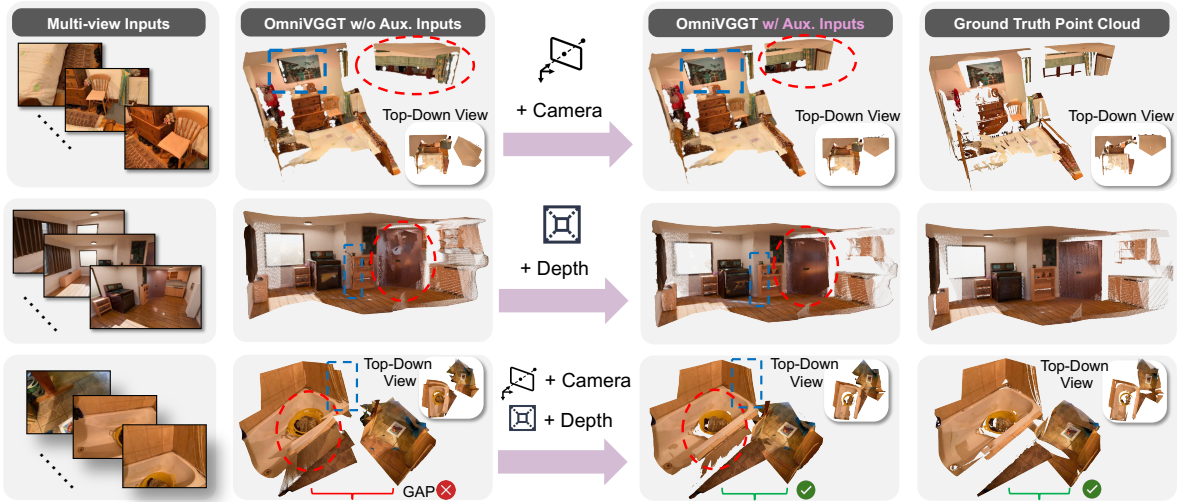


Figure 3. **Visual Results of OmniVGGT with Different Auxiliary Information.** (Top) Camera information help correct challenging scenarios with little or no overlap. (Middle) Providing depth information leads to more accurate local geometry, such as on door surfaces. (Bottom) When both depth and camera information are provided, the relative distances and viewing angles are properly corrected.

static and dynamic scenes. Such a diverse composition ensures strong generalization capability for OmniVGGT. See appendix for the full dataset details.

Implementation Details. Our model architecture follows VGGT [63] with $L = 24$ AA blocks. Camera GeoAdapter has $(L + 1)$ independent camera encoders, each consisting of a single linear layer. The depth GeoAdapter has only one depth encoder, which consists of a single convolutional layer with a kernel size of 14, patchifying the depth maps into the same dimension as the spatial tokens. Our lightweight GeoAdapter introduces only 26.8M additional parameters. The training runs end-to-end on 32 NVIDIA A100 GPUs over ten days. Gradient checkpointing is used to optimize memory usage.

Metrics. For *depth evaluation*, we use absolute relative error (Abs Rel) and percentage of inlier points $\delta < 1.25$ fol-

lowing [19]. For *camera pose estimation*, we use relative rotation accuracy (RRA) and relative translation accuracy (RTA) as the metrics following [63], which calculate the relative angular errors in rotation and translation, respectively, for each image pair. In addition, AUC is the area under the accuracy threshold curve of the minimum values between RRA and RTA across varying thresholds. For *3D reconstruction*, we use the standard metrics of Accuracy (Acc), Completeness (Comp), and Normal Consistency (NC), following [60, 65, 66].

5.1. Auxiliary Information Guidance

We perform a zero-shot evaluation on the Sintel dataset [8] to showcase the effect of injecting auxiliary information at arbitrary ratios on camera pose and depth prediction. Specifically, we randomly sample 10 images from 100

scenes. All images are resized to a fixed width of 518 pixels, with the aspect ratio adjusted to match the closest ratio used during training. The reported results are averaged over all samples. As shown in Table 1, our method outperforms the VGGT baseline even in the auxiliary-free setting, achieving a 0.65 reduction in $\delta < 1.25$ for depth estimation and a 0.46 gain in RRA@5° for pose estimation. Moreover, our method demonstrates strong scalability, showing consistent improvements across all metrics as the proportion of available ground-truth camera or depth information increases. For instance, incorporating only 30% of the depth information reduces the Abs. Rel error by 69.71%. Furthermore, when incorporating auxiliary depth information, our method also achieves notable gains in pose estimation. For example, with 100% of the depth information injected, the pose estimation improves by 6.33 in AUC@30°. This further demonstrates that our approach enhances the accuracy of spatial representations through auxiliary cues, rather than merely learning a direct mapping from input to output. Qualitative results in Fig. 3 further confirm this observation: providing auxiliary pose information not only leads to more accurate pose predictions but also yields more faithful geometric representations. Meanwhile, supplying auxiliary depth information enhances geometric details and improves inter-view pose alignment accuracy.

5.2. Depth Estimation

Mono-Depth Estimation. We first evaluate monocular depth estimation on Sintel [8], Bonn [41], and NYU-v2 [54] datasets following the previous benchmark [64, 75], which cover dynamic and static, indoor and outdoor, realistic and synthetic data. These datasets are not used for training and are suitable for benchmarking the zero-shot performance across different domains.

As shown in Table 2, our method achieves superior performance on both the Sintel and NYU-v2 datasets, surpassing the baseline by 0.5 and 1.0 in $\delta < 1.25$ metric even without any auxiliary information. Moreover, compared to Pow3R [22], our method achieves greater performance gains when incorporating auxiliary depth information (w/ D), reaching nearly perfect accuracy (99.9% in $\delta < 1.25$) on both the Bonn and NYU-v2 datasets. This demonstrates that our GeoAdapter effectively injects auxiliary information into the spatial representations, thereby enhancing the performance of downstream tasks.

Multi-View Depth Estimation. Following Robust-MVD [52], we evaluate the multi-view depth performance on the ScanNet [12], ETH3D [51], DTU [1], and Tanks and Temples [26] datasets.

The detailed results are presented in Table 3, where our method consistently outperforms prior approaches in both accuracy and robustness. Without any auxiliary information, it already achieves superior results on ScanNet and

Table 2. **Single-frame Depth Evaluation.** We report the performance on Sintel, Bonn, and NYU-v2 (static) datasets. ‘w/ D’ indicates that 100% depth maps are provided.

Method	Sintel		Bonn		NYU-v2	
	Abs Rel ↓	$\delta < 1.25$ ↑	Abs Rel ↓	$\delta < 1.25$ ↑	Abs Rel ↓	$\delta < 1.25$ ↑
VGGT [63]	0.271	67.7	0.053	97.3	0.060	94.8
Fast3R [69]	0.502	52.8	0.192	77.3	0.099	88.9
DUSi3R [66]	0.424	58.7	0.141	82.5	0.080	90.7
MASt3R [29]	0.340	60.4	0.142	82.0	0.129	84.9
MonST3R [75]	0.358	54.8	0.076	93.9	0.102	88.0
Spann3R [60]	0.470	53.9	0.118	85.9	0.122	84.9
CUT3R [65]	0.428	55.4	0.063	96.2	0.086	90.9
Pow3R [22]	0.464	54.8	0.132	84.2	0.094	89.6
Pow3R w/ D [22]	<u>0.150</u>	<u>87.4</u>	<u>0.009</u>	<u>99.7</u>	<u>0.009</u>	<u>99.8</u>
OmniVGGT	0.250	68.2	0.064	95.5	0.058	95.8
OmniVGGT w/ D	0.107	90.2	0.008	99.9	0.008	99.9

comparable or better scores on ETH3D and DTU. Furthermore, incorporating auxiliary depth supervision (w/ D) yields a pronounced improvement across all datasets, reaching near-perfect correlation on ETH3D and DTU.

5.3. Camera Pose Estimation

We evaluate OmniVGGT for camera pose prediction on Co3Dv2 [46] and RealEstate10K [77]. Specifically, we randomly select 10 images from each scene and evaluate them using the standard AUC@30° metric following [61].

As shown in Table 4, in the RGB-only setting, OmniVGGT outperforms the state-of-the-art method VGGT, and significantly surpasses all other baselines. Furthermore, when auxiliary inputs are available, OmniVGGT demonstrates consistent performance gains, outperforming the advanced auxiliary-aware method Pow3R, by up to 16% on Re10K. Remarkably, this superior performance is achieved with unprecedented flexibility and efficiency: OmniVGGT is the first to accept an arbitrary number of auxiliary inputs, yet it operates approximately 30× faster than Pow3R.

5.4. 3D Reconstruction

We evaluate scene-level 3D reconstruction on the 7-Scenes [53] benchmark following previous works [60, 65, 66]. In this benchmark, each scene consists of 3–5 sparsely captured frames with minimal or no overlap between views.

As shown in Table 5, OmniVGGT achieves competitive performance with existing state-of-the-art VGGT in the RGB-only setting. Furthermore, it significantly boosts performance when auxiliary inputs (e.g., depth and camera parameters) are available, substantially outperforming all existing baselines. Notably, the inclusion of camera parameters (OmniVGGT w/ (K+RT)) yields a remarkable 65.4% performance gain (metric improving from 0.104 to 0.036) over the baseline OmniVGGT. We attribute this to the extreme image sparsity of the 7-Scenes dataset, as illustrated in Fig. 4. This sparsity makes from-scratch camera pose estimation exceptionally difficult and creates a severe perfor-

Table 3. **Multi-view Depth Evaluation.** (Parentheses) denote training on data from the same domain. “K”, “RT”, and “D” denote intrinsic, relative pose, and depth information, respectively. The best and second best results are **bold** and underlined respectively.

Method	GT	Align	ScanNet [12]		ETH3D [51]		DTU [1]		T&T [26]		Average	
	Range	Method	rel↓	τ ↑	rel↓	τ ↑	rel↓	τ ↑	rel↓	τ ↑	rel↓	τ ↑
COLMAP [49, 50] (K+RT)	×	×	14.6	34.2	16.4	55.1	0.7	96.5	2.7	95.0	8.6	70.2
COLMAP Dense [49, 50] (K+RT)	×	×	38.0	22.5	89.8	23.2	20.8	69.3	25.7	76.4	43.6	47.9
MVSNet [70] (K+RT)	✓	×	22.7	20.9	21.6	35.6	(1.8)	(86.7)	6.5	74.6	12.3	11.1
Vis-MVSNet [74] (K+RT)	✓	×	8.9	33.5	10.8	43.3	1.8	87.4	4.1	7.2	6.4	42.9
MVS-Former++ (K+RT)	✓	×	15.2	21.9	21.4	32.5	(1.2)	(91.9)	7.6	71.5	10.8	8.5
CER-MVS [11] (K+RT)	×	×	21.1	24.3	11.7	47.5	4.1	71.3	6.4	82.1	10.8	56.3
DUST3R [66]	×	med	(3.1)	(71.8)	3.0	76.0	3.9	68.6	3.3	75.1	3.3	72.9
Pow3R [22]	×	med	(3.2)	(68.8)	3.0	74.7	3.0	74.3	3.3	76.6	3.1	73.6
VGGT [63]	×	med	(3.7)	(70.0)	1.7	87.2	0.9	95.4	1.7	90.6	2.0	85.8
OmniVGGT	×	med	(3.6)	(72.3)	1.8	87.5	1.1	93.9	1.8	90.0	2.1	85.9
Pow3R [22] w/ (K+RT)	×	med	(3.1)	(71.4)	2.8	77.1	1.5	91.1	3.2	78.2	2.7	79.5
OmniVGGT w/ (K+RT)	×	med	(3.7)	(72.2)	1.8	87.8	1.2	93.6	1.8	89.9	2.1	85.9
OmniVGGT w/ D	×	med	<u>(2.3)</u>	<u>(85.6)</u>	0.5	<u>98.7</u>	<u>0.3</u>	99.5	<u>0.9</u>	<u>95.5</u>	<u>1.0</u>	<u>94.8</u>
OmniVGGT w/ (K+RT+D)	×	med	(2.2)	(86.7)	0.5	98.7	0.3	<u>99.4</u>	0.9	95.6	1.0	95.1

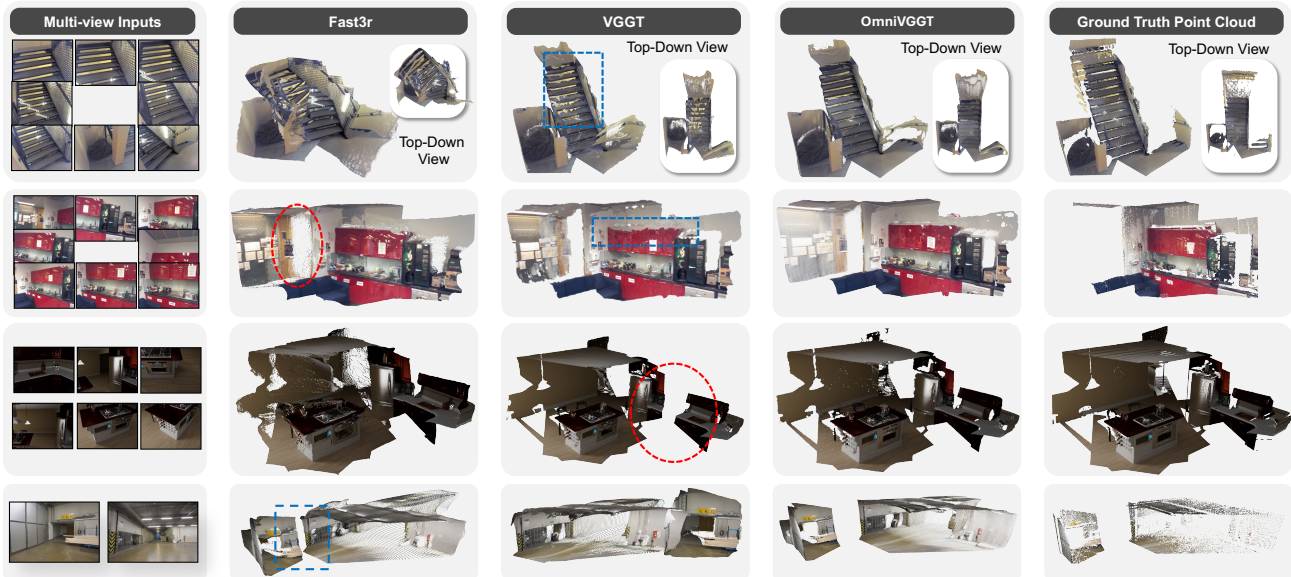


Figure 4. **Visual Comparisons on 7-Scenes [53], NRGBD [4], and ETH3D [51] datasets.** OmniVGGT exhibits accurate spatial relationships and geometric consistency, even in extremely challenging cases. More examples can be found in the appendix.

mance bottleneck. Our method effectively overcomes this bottleneck by leveraging the accessible camera pose information, demonstrating its robustness in handling sparse and non-overlapping viewpoints.

5.5. Application on Vision-Language-Action Model

OmniVGGT generates richer and more representative 3D spatial tokens by progressively incorporating auxiliary inputs like depth and pose. This inherent spatial awareness is vital for the VLA model [30, 42], which is required to interact with the physical 3D world and, critically, predict absolute poses for robotic manipulation. Specifically, as shown in Fig. 1, we build upon the Kosmos-VLA 1.6B model [42]

with an FCN action head, where our spatial tokens are injected and fused with the VLM tokens to enhance spatial reasoning. We then finetune the VLA model and evaluate it on the CALVIN dataset [37]. As shown in Table 6, under the ABCD→D setting, our method with auxiliary depth inputs outperforms approaches that incorporate 3D priors via a point encoder by 0.04 in the Avg. Len metric. Under the zero-shot ABC→D setting, our RGB-only variant also surpasses the Kosmos w/ RGB baseline by a large margin of 0.43 in Avg. Len. These results demonstrate that our approach learns richer spatial representations and can be further enhanced by auxiliary inputs to improve robotic manipulation accuracy. See supplement for rollout examples.

Table 4. **Camera Pose Estimation on the RealEstate10K [77] and CO3Dv2 [46] datasets.** Pro means using Procrustes alignment. ‘()’ means not trained on CO3D.

Method	Re10K <i>unseen</i>		CO3Dv2		Time
	AUC@30° (%) ↑	AUC@30° (%) ↑	AUC@30° (%) ↑	AUC@30° (%) ↑	
COLMAP+SPSG [48]	45.2	25.3			~ 15s
PixSfM [32]	49.4	30.1			> 20s
PoseDiff [61]	48.0	66.5			~ 7s
DUST3R [66]	67.7	76.7			~ 7s
MASt3R [29]	76.4	81.8			~ 9s
VGGsfM v2 [62]	78.9	83.4			~ 10s
MV-DUST3R [57]	71.3	(69.5)			~ 0.6s
CUT3R [65]	75.3	82.8			~ 0.6s
FLARE [76]	78.8	83.3			~ 0.5s
Fast3R [69]	72.7	82.5			~ 0.2s
VGGT [63]	85.3	88.2			~ 0.2s
Pow3R (PnP) [17]	62.5	78.5			> 7s
Pow3R (Pro) [22]	62.5	78.5			> 7s
OmniVGGT	85.9	88.4			~ 0.2s
Pow3R w/ K (Pro) [22]	72.5	82.2			> 7s
OmniVGGT w/ D	85.5	91.3			~ 0.2s
OmniVGGT w/ K+RT	88.5	93.4			~ 0.2s

Table 5. **3D reconstruction on the 7-scenes [53] datasets.** "K", "RT", and "D" denote intrinsic, relative pose, and depth information, respectively.

Method	Acc↓		Comp↓		NC↑	
	Mean	Med.	Mean	Med.	Mean	Med.
VGGT [63]	0.087	0.039	0.091	0.039	0.787	0.890
Fast3R [69]	0.164	0.108	0.163	0.080	0.686	0.775
DUST3R-GA [66]	0.146	0.077	0.181	0.067	0.736	0.839
MASt3R-GA [29]	0.185	0.081	0.180	0.069	0.701	0.792
MonST3R-GA [75]	0.248	0.185	0.266	0.167	0.672	0.759
Spann3R [60]	0.298	0.226	0.205	0.112	0.650	0.730
SLAM3R [34]	0.287	0.155	0.226	0.066	0.644	0.720
CUT3R [65]	0.126	0.047	0.154	0.031	0.727	0.834
OmniVGGT	0.104	0.037	0.112	0.031	0.763	0.875
OmniVGGT w/ D	0.085	0.034	0.085	0.027	0.789	0.894
OmniVGGT w/ (K+RT)	0.037	0.017	0.049	0.019	0.778	0.893
OmniVGGT w/ (K+RT+D)	0.036	0.017	0.036	0.017	0.810	0.912

Table 6. Performance comparison of different modality input on CALVIN [37] benchmark. Kosmos-VLA (w/ rgb-d) is a point cloud-based version with a lightweight point cloud encoder [73] while retaining other parts.

Method	Task	Tasks Completed in a Row (%)					Avg. Len. ↑
		1	2	3	4	5	
Kosmos-VLA (w/ rgb)	ABCD→D	92.9	85.4	79.4	74.4	68.1	4.00
Kosmos-VLA (w/ rgb-d)	ABCD→D	93.4	85.8	80.5	75.3	69.2	4.04
Ours (w/ rgb)	ABCD→D	93.8	86.6	81.0	75.5	69.5	4.07
Ours (w/ rgb-d)	ABCD→D	93.7	86.8	81.4	76.7	70.2	4.08
Kosmos-VLA (w/ rgb)	ABC→D	90.1	79.1	69.2	59.6	50.9	3.49
Kosmos-VLA (w/ rgb-d)	ABC→D	93.6	86.0	78.6	72.9	64.8	3.97
Ours (w/ rgb)	ABC→D	93.8	86.9	77.9	70.3	62.2	3.92
Ours (w/ rgb-d)	ABC→D	95.1	87.7	79.2	70.8	63.0	3.96

5.6. Architecture Ablation

We conduct a comprehensive ablation study on GeoAdapter to thoroughly analyze its working mechanism. As shown in Fig. 5, we evaluate three variants: (a) *Replace*, where

Table 7. **Ablation of GeoAdapter architectures.** We compare different GeoAdapter designs on the Sintel [8] dataset.

Architecture	Depth		Camera		
	Abs Rel↓	$\delta < 1.25$ ↑	RRA@5° ↑	RTA@5° ↑	AUC@30° ↑
<i>w/o (K+RT+D) Auxiliary Information</i>					
(a) <i>Replace</i>	0.845	64.74	93.40	30.88	64.74
(b) <i>One-Layer Adapter</i>	0.604	68.74	96.78	44.92	68.74
(c) <i>Depth ZeroConv</i>	0.569	70.71	96.44	51.86	69.70
(d) <i>OmniVGGT</i>	0.558	71.46	96.15	54.01	70.83
<i>w/ (K+RT+D) Auxiliary Information</i>					
(a) <i>Replace</i>	0.655	82.96	97.08	57.61	77.83
(b) <i>One-Layer Adapter</i>	0.133	85.65	99.97	60.89	81.66
(c) <i>Depth ZeroConv</i>	0.505	71.11	99.72	71.66	84.12
(d) <i>OmniVGGT</i>	0.106	85.95	99.97	76.33	85.99

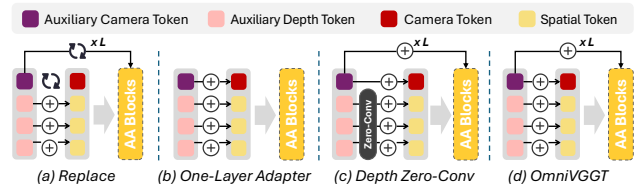


Figure 5. **Visualization of our GeoAdapter module in ablation.**

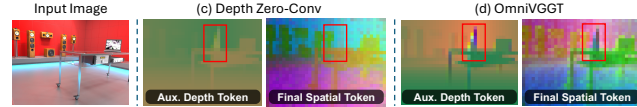


Figure 6. **Token visualization of our GeoAdapter module.** Discriminative areas are highlighted with ‘□’.

the original camera tokens are directly replaced by auxiliary camera tokens in each AA block. (b) *One-Layer Adapter*, where auxiliary camera tokens are only injected once before the AA blocks. (c) *Depth ZeroConv*, where a ZeroConv layer is used for depth information injection.

As shown in Table 7, variant (a) yields suboptimal results in both the RGB-only setting and the full auxiliary information setting, while variant (b) is insufficient to strengthen the correct prior knowledge in the full auxiliary information setting. Regarding (c), the model tends to interpret the auxiliary depth information as noise, leading to limited performance improvement. As illustrated by the PCA visualization in Fig. 6, the (d) configuration preserves more complete and discriminative auxiliary depth information than (c), leading to a more accurate spatial representation.

6. Conclusion

We propose OmniVGGT, a unified feed-forward model capable of handling diverse input modalities for various 3D tasks. Our model flexibly accommodates casual inputs, including arbitrary numbers of images, auxiliary information, and input combinations. It achieves state-of-the-art performance across multiple tasks (from reconstruction to robotics) while maintaining high inference efficiency. Our findings demonstrate that integrating multi-modalities information within a unified architecture can significantly advance the development of 3D foundation models.

References

- [1] Henrik Aanæs, Rasmus Ramsbøl Jensen, George Vogiatzis, Engin Tola, and Anders Bjarholm Dahl. Large-scale data for multiple-view stereopsis. *International Journal of Computer Vision*, 120(2):153–168, 2016. 6, 7, 4
- [2] Josh Achiam, Steven Adler, Sandhini Agarwal, Lama Ahmad, Ilge Akkaya, Florencia Leoni Aleman, Diogo Almeida, Janko Altmerschmidt, Sam Altman, Shyamal Anadkat, et al. Gpt-4 technical report. *arXiv preprint arXiv:2303.08774*, 2023. 2
- [3] Eduardo Arnold, Jamie Wynn, Sara Vicente, Guillermo Garcia-Hernando, Aron Monszpart, Victor Prisacariu, Daniyar Turmukhambetov, and Eric Brachmann. Map-free visual relocalization: Metric pose relative to a single image. In *European Conference on Computer Vision*, pages 690–708. Springer, 2022. 2, 4, 1
- [4] Dejan Azinović, Ricardo Martin-Brualla, Dan B Goldman, Matthias Nießner, and Justus Thies. Neural rgb-d surface reconstruction. In *Proceedings of the IEEE/CVF Conference on Computer Vision and Pattern Recognition*, pages 6290–6301, 2022. 7, 2, 4, 5
- [5] Yanqi Bao, Tianyu Ding, Jing Huo, Yaoli Liu, Yuxin Li, Wenbin Li, Yang Gao, and Jiebo Luo. 3d gaussian splatting: Survey, technologies, challenges, and opportunities. *IEEE Transactions on Circuits and Systems for Video Technology*, 35(7):6832–6852, 2025. 2
- [6] Gilad Baruch, Zhuoyuan Chen, Afshin Dehghan, Tal Dimry, Yuri Feigin, Peter Fu, Thomas Gebauer, Brandon Joffe, Daniel Kurz, Arik Schwartz, et al. Arkitscenes: A diverse real-world dataset for 3d indoor scene understanding using mobile rgb-d data. *arXiv preprint arXiv:2111.08897*, 2021. 4, 1, 2, 3
- [7] Zuria Bauer, Francisco Gomez-Donoso, Edmanuel Cruz, Sergio Orts-Escolano, and Miguel Cazorla. Uasol, a large-scale high-resolution outdoor stereo dataset. *Scientific data*, 6(1):162, 2019. 4, 1, 2
- [8] Daniel J Butler, Jonas Wulff, Garrett B Stanley, and Michael J Black. A naturalistic open source movie for optical flow evaluation. In *European conference on computer vision*, pages 611–625. Springer, 2012. 5, 6, 8, 2
- [9] Johann Cabon, Naila Murray, and Martin Humenberger. Virtual kitti 2. *arXiv preprint arXiv:2001.10773*, 2020. 4, 1, 2
- [10] Holger Caesar, Varun Bankiti, Alex H. Lang, Sourabh Vora, Venice Erin Liong, Qiang Xu, Anush Krishnan, Yu Pan, Giancarlo Baldan, and Oscar Beijbom. nuscenes: A multi-modal dataset for autonomous driving. In *Proceedings of the IEEE/CVF Conference on Computer Vision and Pattern Recognition (CVPR)*, pages 11621–11631, 2020. 2
- [11] Chenjie Cao, Xinlin Ren, and Yanwei Fu. Mvsformer++: Revealing the devil in transformer’s details for multi-view stereo. *arXiv preprint arXiv:2401.11673*, 2024. 2, 7, 4
- [12] Angela Dai, Angel X Chang, Manolis Savva, Maciej Halber, Thomas Funkhouser, and Matthias Nießner. Scannet: Richly-annotated 3d reconstructions of indoor scenes. In *Proceedings of the IEEE conference on computer vision and pattern recognition*, pages 5828–5839, 2017. 4, 6, 7, 1, 2
- [13] Angela Dai, Matthias Nießner, Michael Zollhöfer, Shahram Izadi, and Christian Theobalt. Bundlefusion: Real-time globally consistent 3d reconstruction using on-the-fly surface reintegration. *ACM Transactions on Graphics (Proc. SIGGRAPH)*, 36(4), 2017. 2
- [14] Ben Fei, Jingyi Xu, Rui Zhang, Qingyuan Zhou, Weidong Yang, and Ying He. 3d gaussian splatting as a new era: A survey. *IEEE Transactions on Visualization and Computer Graphics*, 31(8):4429–4449, 2025. 2
- [15] Kyle Gao, Yina Gao, Hongjie He, Dening Lu, Linlin Xu, and Jonathan Li. Nerf: Neural radiance field in 3d vision, a comprehensive review. *arXiv preprint arXiv:2210.00379*, 2022. 2
- [16] Klaus Greff, Francois Belletti, Lucas Beyer, Carl Doersch, Yilun Du, Daniel Duckworth, David J Fleet, Dan Gnanaprasam, Florian Golemo, Charles Herrmann, et al. Kubric: A scalable dataset generator. In *Proceedings of the IEEE/CVF conference on computer vision and pattern recognition*, pages 3749–3761, 2022. 4, 1, 2
- [17] Richard Hartley and Andrew Zisserman. *Multiple view geometry in computer vision*. Cambridge university press, 2003. 8
- [18] Jiarui Hu, Xianhao Chen, Boyin Feng, Guanglin Li, Liangjing Yang, Hujun Bao, Guofeng Zhang, and Zhaopeng Cui. Cg-slam: Efficient dense rgb-d slam in a consistent uncertainty-aware 3d gaussian field. In *Computer Vision – ECCV 2024, Lecture Notes in Computer Science*, pages 93–112. Springer, 2024. 2
- [19] Wenbo Hu, Xiangjun Gao, Xiaoyu Li, Sijie Zhao, Xiaodong Cun, Yong Zhang, Long Quan, and Ying Shan. Depthcrafter: Generating consistent long depth sequences for open-world videos. In *Proceedings of the Computer Vision and Pattern Recognition Conference*, pages 2005–2015, 2025. 2, 5
- [20] Yafei Hu, Quanting Xie, Vidhi Jain, Jonathan Francis, Jay Patrikar, Nikhil Keetha, Seungchan Kim, Yaqi Xie, Tianyi Zhang, Hao-Shu Fang, et al. Toward general-purpose robots via foundation models: A survey and meta-analysis. *arXiv preprint arXiv:2312.08782*, 2023. 2
- [21] Po-Han Huang, Kevin Matzen, Johannes Kopf, Narendra Ahuja, and Jia-Bin Huang. Deepmvs: Learning multi-view stereopsis. In *Proceedings of the IEEE conference on computer vision and pattern recognition*, pages 2821–2830, 2018. 2, 4, 1
- [22] Wonbong Jang, Philippe Weinzaepfel, Vincent Leroy, Lourdes Agapito, and Jerome Revaud. Pow3r: Empowering unconstrained 3d reconstruction with camera and scene priors. In *Proceedings of the Computer Vision and Pattern Recognition Conference*, pages 1071–1081, 2025. 2, 6, 7, 8, 1, 4
- [23] Nikita Karaev, Ignacio Rocco, Benjamin Graham, Natalia Neverova, Andrea Vedaldi, and Christian Rupprecht. Dynamicstereo: Consistent dynamic depth from stereo videos. In *Proceedings of the IEEE/CVF Conference on Computer Vision and Pattern Recognition*, pages 13229–13239, 2023. 4, 1, 2
- [24] Nikhil Keetha, Jay Karhade, Krishna Murthy Jatavallabhula, Gengshan Yang, Sebastian Scherer, Deva Ramanan, and

- Jonathon Luiten. Splatam: Splat track & map 3d gaussians for dense rgb-d slam. In *Proceedings of the IEEE/CVF Conference on Computer Vision and Pattern Recognition*, pages 21357–21366, 2024. 2
- [25] Bernhard Kerbl, Georgios Kopanas, Thomas Leimkühler, and George Drettakis. 3d gaussian splatting for real-time radiance field rendering. *ACM Trans. Graph.*, 42(4):139–1, 2023. 2
- [26] Arno Knapitsch, Jaesik Park, Qian-Yi Zhou, and Vladlen Koltun. Tanks and temples: Benchmarking large-scale scene reconstruction. *ACM Transactions on Graphics (ToG)*, 36(4):1–13, 2017. 6, 7, 4
- [27] Yushi Lan, Yihang Luo, Fangzhou Hong, Shangchen Zhou, Honghua Chen, Zhaoyang Lyu, Shuai Yang, Bo Dai, Chen Change Loy, and Xingang Pan. Stream3r: Scalable sequential 3d reconstruction with causal transformer. *arXiv preprint arXiv:2508.10893*, 2025. 3
- [28] Alex H. Lang, Sourabh Vora, Holger Caesar, Lubing Zhou, Jiong Yang, and Oscar Beijbom. Pointpillars: Fast encoders for object detection from point clouds. In *Proceedings of the IEEE/CVF Conference on Computer Vision and Pattern Recognition (CVPR)*, pages 12697–12705, 2019. 2
- [29] Vincent Leroy, Yohann Cabon, and Jérôme Revaud. Grounding image matching in 3d with mast3r. In *European Conference on Computer Vision*, pages 71–91. Springer, 2024. 2, 6, 8, 4
- [30] Xinghang Li, Peiyan Li, Minghuan Liu, Dong Wang, Jirong Liu, Bingyi Kang, Xiao Ma, Tao Kong, Hanbo Zhang, and Huaping Liu. Towards generalist robot policies: What matters in building vision-language-action models. *arXiv preprint arXiv:2412.14058*, 2024. 7
- [31] Zhengqi Li and Noah Snavely. Megadepth: Learning single-view depth prediction from internet photos. In *Proceedings of the IEEE conference on computer vision and pattern recognition*, pages 2041–2050, 2018. 2, 4, 1
- [32] Philipp Lindenberger, Paul-Edouard Sarlin, Viktor Larsson, and Marc Pollefeys. Pixel-perfect structure-from-motion with featuremetric refinement. In *Proceedings of the IEEE/CVF international conference on computer vision*, pages 5987–5997, 2021. 8
- [33] Lu Ling, Yichen Sheng, Zhi Tu, Wentian Zhao, Cheng Xin, Kun Wan, Lantao Yu, Qianyu Guo, Zixun Yu, Yawen Lu, et al. D13dv-10k: A large-scale scene dataset for deep learning-based 3d vision. In *Proceedings of the IEEE/CVF Conference on Computer Vision and Pattern Recognition*, pages 22160–22169, 2024. 4, 1, 2
- [34] Yuzheng Liu, Siyan Dong, Shuzhe Wang, Yingda Yin, Yan-chao Yang, Qingnan Fan, and Baoquan Chen. Slam3r: Real-time dense scene reconstruction from monocular rgb videos. In *Proceedings of the Computer Vision and Pattern Recognition Conference*, pages 16651–16662, 2025. 8, 4
- [35] Yang Liu, Chuanchen Luo, Zimo Tang, Junran Peng, and Zhaoxiang Zhang. Vggt-x: When vggt meets dense novel view synthesis. *arXiv preprint arXiv:2509.25191*, 2025. 3
- [36] Dominic Maggio, Hyungtae Lim, and Luca Carlone. Vggt-slam: Dense rgb slam optimized on the sl (4) manifold. *arXiv preprint arXiv:2505.12549*, 2025. 3
- [37] Oier Mees, Lukas Hermann, Erick Rosete-Beas, and Wolfram Burgard. Calvin: A benchmark for language-conditioned policy learning for long-horizon robot manipulation tasks. *IEEE Robotics and Automation Letters (RA-L)*, 7(3):7327–7334, 2022. 7, 8
- [38] Lukas Mehl, Jenny Schmalfluss, Azin Jahedi, Yaroslava Nali-vayko, and Andrés Bruhn. Spring: A high-resolution high-detail dataset and benchmark for scene flow, optical flow and stereo. In *Proceedings of the IEEE/CVF Conference on Computer Vision and Pattern Recognition*, pages 4981–4991, 2023. 4, 1, 2
- [39] Ben Mildenhall, Pratul P Srinivasan, Matthew Tancik, Jonathan T Barron, Ravi Ramamoorthi, and Ren Ng. Nerf: Representing scenes as neural radiance fields for view synthesis. *Communications of the ACM*, 65(1):99–106, 2021. 2
- [40] Maxime Oquab, Timothée Darcet, Théo Moutakanni, Huy Vo, Marc Szafraniec, Vasil Khalidov, Pierre Fernandez, Daniel Haziza, Francisco Massa, Alaaeldin El-Nouby, et al. Dinov2: Learning robust visual features without supervision. *arXiv preprint arXiv:2304.07193*, 2023. 3
- [41] Emanuele Palazzolo, Jens Behley, Philipp Lottes, Philippe Giguere, and Cyrill Stachniss. Refusion: 3d reconstruction in dynamic environments for rgb-d cameras exploiting residuals. In *2019 IEEE/RSJ International Conference on Intelligent Robots and Systems (IROS)*, pages 7855–7862. IEEE, 2019. 6
- [42] Zhiliang Peng, Wenhui Wang, Li Dong, Yaru Hao, Shaohan Huang, Shuming Ma, and Furu Wei. Kosmos-2: Grounding multimodal large language models to the world. *arXiv preprint arXiv:2306.14824*, 2023. 7
- [43] Zhexi Peng, Tianjia Shao, Yong Liu, Jingke Zhou, Yin Yang, Jingdong Wang, and Kun Zhou. Rtg-slam: Real-time 3d reconstruction at scale using gaussian splatting. In *ACM SIGGRAPH 2024 Conference Papers*, 2024. Also available as arXiv:2404.19706. 2
- [44] Santhosh Kumar Ramakrishnan, Aaron Gokaslan, Erik Wijmans, Oleksandr Maksymets, Alexander Clegg, John M Turner, Eric Undersander, Wojciech Galuba, Andrew Westbury, Angel X Chang, Manolis Savva, Yili Zhao, and Dhruv Batra. Habitat-matterport 3d dataset (HM3d): 1000 large-scale 3d environments for embodied AI. In *Thirty-fifth Conference on Neural Information Processing Systems Datasets and Benchmarks Track*, 2021. 4, 1, 2
- [45] René Ranftl, Alexey Bochkovskiy, and Vladlen Koltun. Vision transformers for dense prediction. In *Proceedings of the IEEE/CVF international conference on computer vision*, pages 12179–12188, 2021. 3
- [46] Jeremy Reizenstein, Roman Shapovalov, Philipp Henzler, Luca Sbordone, Patrick Labatut, and David Novotny. Common objects in 3d: Large-scale learning and evaluation of real-life 3d category reconstruction. In *Proceedings of the IEEE/CVF international conference on computer vision*, pages 10901–10911, 2021. 6, 8
- [47] Mike Roberts, Jason Ramapuram, Anurag Ranjan, Atulit Kumar, Miguel Angel Bautista, Nathan Paczan, Russ Webb, and Joshua M Susskind. Hypersim: A photorealistic synthetic dataset for holistic indoor scene understanding. In

- Proceedings of the IEEE/CVF international conference on computer vision*, pages 10912–10922, 2021. 4, 1, 2
- [48] Paul-Edouard Sarlin, Daniel DeTone, Tomasz Malisiewicz, and Andrew Rabinovich. Superglue: Learning feature matching with graph neural networks. In *Proceedings of the IEEE/CVF conference on computer vision and pattern recognition*, pages 4938–4947, 2020. 8
- [49] Johannes L Schonberger and Jan-Michael Frahm. Structure-from-motion revisited. In *Proceedings of the IEEE conference on computer vision and pattern recognition*, pages 4104–4113, 2016. 7, 4
- [50] Johannes L Schönberger, Enliang Zheng, Jan-Michael Frahm, and Marc Pollefeys. Pixelwise view selection for unstructured multi-view stereo. In *European conference on computer vision*, pages 501–518. Springer, 2016. 7, 4
- [51] Thomas Schops, Johannes L Schonberger, Silvano Galliani, Torsten Sattler, Konrad Schindler, Marc Pollefeys, and Andreas Geiger. A multi-view stereo benchmark with high-resolution images and multi-camera videos. In *Proceedings of the IEEE conference on computer vision and pattern recognition*, pages 3260–3269, 2017. 6, 7, 2, 4, 5
- [52] Philipp Schröppel, Jan Bechtold, Artemij Amiranashvili, and Thomas Brox. A benchmark and a baseline for robust multi-view depth estimation. In *2022 International Conference on 3D Vision (3DV)*, pages 637–645. IEEE, 2022. 6
- [53] Jamie Shotton, Ben Glocker, Christopher Zach, Shahram Izadi, Antonio Criminisi, and Andrew Fitzgibbon. Scene coordinate regression forests for camera relocalization in rgb-d images. In *Proceedings of the IEEE conference on computer vision and pattern recognition*, pages 2930–2937, 2013. 6, 7, 8, 2, 4, 5
- [54] Nathan Silberman, Derek Hoiem, Pushmeet Kohli, and Rob Fergus. Indoor segmentation and support inference from rgb-d images. In *European conference on computer vision*, pages 746–760. Springer, 2012. 6, 2
- [55] Pei Sun, Henrik Kretzschmar, Xerxes Dotiwalla, Aurelien Chouard, Vijaysai Patnaik, Paul Tsui, James Guo, Yin Zhou, Yuning Chai, Benjamin Caine, Vijay Vasudevan, Wei Han, Jiquan Ngiam, Hang Zhao, Aleksei Timofeev, Scott Ettinger, Maxim Krivokon, Amy Gao, Aditya Joshi, Yu Zhang, Jonathon Shlens, Zhifeng Chen, and Dragomir Anguelov. Scalability in perception for autonomous driving: Waymo open dataset. In *Proceedings of the IEEE/CVF Conference on Computer Vision and Pattern Recognition (CVPR)*, pages 2446–2454, 2020. 2
- [56] Pei Sun, Henrik Kretzschmar, Xerxes Dotiwalla, Aurelien Chouard, Vijaysai Patnaik, Paul Tsui, James Guo, Yin Zhou, Yuning Chai, Benjamin Caine, et al. Scalability in perception for autonomous driving: Waymo open dataset. In *Proceedings of the IEEE/CVF conference on computer vision and pattern recognition*, pages 2446–2454, 2020. 4, 1, 2
- [57] Zhenggang Tang, Yuchen Fan, Dilin Wang, Hongyu Xu, Rakesh Ranjan, Alexander Schwing, and Zhicheng Yan. Mv-dust3r+: Single-stage scene reconstruction from sparse views in 2 seconds. In *Proceedings of the Computer Vision and Pattern Recognition Conference*, pages 5283–5293, 2025. 8
- [58] Fabio Tosi, Yiyi Liao, Carolin Schmitt, and Andreas Geiger. Smd-nets: Stereo mixture density networks. In *Proceedings of the IEEE/CVF conference on computer vision and pattern recognition*, pages 8942–8952, 2021. 4, 1, 2
- [59] Guangming Wang, Lei Pan, Songyou Peng, Shaohui Liu, Chenfeng Xu, Yanzi Miao, Wei Zhan, Masayoshi Tomizuka, Marc Pollefeys, and Hesheng Wang. Nerfs in robotics: A survey. *The International Journal of Robotics Research*, page 02783649251374246, 2024. 2
- [60] Hengyi Wang and Lourdes Agapito. 3d reconstruction with spatial memory. *arXiv preprint arXiv:2408.16061*, 2024. 5, 6, 8, 4
- [61] Jianyuan Wang, Christian Rupprecht, and David Novotny. Posediffusion: Solving pose estimation via diffusion-aided bundle adjustment. In *Proceedings of the IEEE/CVF International Conference on Computer Vision*, pages 9773–9783, 2023. 2, 6, 8
- [62] Jianyuan Wang, Nikita Karaev, Christian Rupprecht, and David Novotny. Vggsfm: Visual geometry grounded deep structure from motion. In *Proceedings of the IEEE/CVF conference on computer vision and pattern recognition*, pages 21686–21697, 2024. 4, 8
- [63] Jianyuan Wang, Minghao Chen, Nikita Karaev, Andrea Vedaldi, Christian Rupprecht, and David Novotny. Vggt: Visual geometry grounded transformer. In *Proceedings of the Computer Vision and Pattern Recognition Conference*, pages 5294–5306, 2025. 2, 3, 4, 5, 6, 7, 8, 1
- [64] Qianqian Wang, Yifei Zhang, Aleksander Holynski, Alexei A Efros, and Angjoo Kanazawa. Continuous 3d perception model with persistent state. In *Proceedings of the Computer Vision and Pattern Recognition Conference*, pages 10510–10522, 2025. 6
- [65] Qianqian Wang, Yifei Zhang, Aleksander Holynski, Alexei A Efros, and Angjoo Kanazawa. Continuous 3d perception model with persistent state. In *Proceedings of the Computer Vision and Pattern Recognition Conference*, pages 10510–10522, 2025. 2, 5, 6, 8, 4
- [66] Shuzhe Wang, Vincent Leroy, Yohann Cabon, Boris Chidlovskii, and Jerome Revaud. Dust3r: Geometric 3d vision made easy. In *Proceedings of the IEEE/CVF Conference on Computer Vision and Pattern Recognition*, pages 20697–20709, 2024. 2, 5, 6, 7, 8, 1, 4
- [67] Wenshan Wang, DeLong Zhu, Xiangwei Wang, Yaoyu Hu, Yuheng Qiu, Chen Wang, Yafei Hu, Ashish Kapoor, and Sebastian Scherer. Tartanair: A dataset to push the limits of visual slam. In *2020 IEEE/RSJ International Conference on Intelligent Robots and Systems (IROS)*, pages 4909–4916. IEEE, 2020. 4, 1, 2
- [68] Hongchi Xia, Yang Fu, Sifei Liu, and Xiaolong Wang. Rgb-d objects in the wild: Scaling real-world 3d object learning from rgb-d videos. In *Proceedings of the IEEE/CVF Conference on Computer Vision and Pattern Recognition*, pages 22378–22389, 2024. 4, 1, 2
- [69] Jianing Yang, Alexander Sax, Kevin J Liang, Mikael Henaff, Hao Tang, Ang Cao, Joyce Chai, Franziska Meier, and Matt Feiszli. Fast3r: Towards 3d reconstruction of 1000+ images in one forward pass. In *Proceedings of the Computer Vision*

- and *Pattern Recognition Conference*, pages 21924–21935, 2025. 6, 8, 4
- [70] Yao Yao, Zixin Luo, Shiwei Li, Tian Fang, and Long Quan. Mvsnet: Depth inference for unstructured multi-view stereo. In *Proceedings of the European conference on computer vision (ECCV)*, pages 767–783, 2018. 2, 7, 4
- [71] Yao Yao, Zixin Luo, Shiwei Li, Jingyang Zhang, Yufan Ren, Lei Zhou, Tian Fang, and Long Quan. Blendedmvs: A large-scale dataset for generalized multi-view stereo networks. In *Proceedings of the IEEE/CVF conference on computer vision and pattern recognition*, pages 1790–1799, 2020. 2, 4, 1
- [72] Chandan Yeshwanth, Yueh-Cheng Liu, Matthias Nießner, and Angela Dai. Scannet++: A high-fidelity dataset of 3d indoor scenes. In *Proceedings of the IEEE/CVF International Conference on Computer Vision*, pages 12–22, 2023. 4, 1, 2
- [73] Yanjie Ze, Zixuan Chen, Wenhao Wang, Tianyi Chen, Xialin He, Ying Yuan, Xue Bin Peng, and Jiajun Wu. Generalizable humanoid manipulation with 3d diffusion policies, 2025. 8
- [74] Jingyang Zhang, Yao Yao, Shiwei Li, Zixin Luo, and Tian Fang. Visibility-aware multi-view stereo network. *arXiv preprint arXiv:2008.07928*, 2020. 7, 4
- [75] Junyi Zhang, Charles Herrmann, Junhwa Hur, Varun Jampani, Trevor Darrell, Forrester Cole, Deqing Sun, and Ming-Hsuan Yang. Monst3r: A simple approach for estimating geometry in the presence of motion. *arXiv preprint arXiv:2410.03825*, 2024. 6, 8, 4
- [76] Shangzhan Zhang, Jianyuan Wang, Yinghao Xu, Nan Xue, Christian Rupprecht, Xiaowei Zhou, Yujun Shen, and Gordon Wetzstein. Flare: Feed-forward geometry, appearance and camera estimation from uncalibrated sparse views. In *Proceedings of the Computer Vision and Pattern Recognition Conference*, pages 21936–21947, 2025. 8
- [77] Tinghui Zhou, Richard Tucker, John Flynn, Graham Fyffe, and Noah Snavely. Stereo magnification: Learning view synthesis using multiplane images. *arXiv preprint arXiv:1805.09817*, 2018. 6, 8
- [78] Yang Zhou, Yifan Wang, Jianjun Zhou, Wenzheng Chang, Haoyu Guo, Zizun Li, Kaijing Ma, Xinyue Li, Yating Wang, Haoyi Zhu, Mingyu Liu, Dingning Liu, Jiange Yang, Zhoujie Fu, Junyi Chen, Chunhua Shen, Jiangmiao Pang, Kaipeng Zhang, and Tong He. Omniworld: A multi-domain and multi-modal dataset for 4d world modeling, 2025. 2, 3
- [79] Dong Zhuo, Wenzhao Zheng, Jiahe Guo, Yuqi Wu, Jie Zhou, and Jiwen Lu. Streaming 4d visual geometry transformer. *arXiv preprint arXiv:2507.11539*, 2025. 3

OmniVGGT: Omni-Modality Driven Visual Geometry Grounded Transformer

Supplementary Material

A. Appendix

A.1. Dataset Details

We train our model on 19 datasets that contain a diverse range of scene types, including: ARKitScenes [6], BlendedMVS [71], DL3DV [33], Dynamic Replica [23], HyperSim [47], Kubric [16], MapFree [3], MegaDepth [31], Matterport 3D [44], MVS-Synth [21], ScanNet [12], ScanNet++ [72], Spring [38], TartanAir [67], UASOL [7], Unreal 4K [58], Virtual KITTI [9], Waymo [56], WildRGBD [68]. We modified the official DUST3R [66] dataloader script to adapt it for the VGGT [63] training process. Table 8 summarizes the statistics of the datasets we used. During training, in each epoch, we sample a fixed total number of samples from the training datasets, with their proportions indicated by the “ratio” column in the table. Note that the number of images may differ from the full official release.

A.2. More Implementation details

Training Objective. In OmniVGGT, all input images, together with the available camera parameters and depth maps (if provided), are fed into the network \mathcal{G} , which predicts in an end-to-end manner the 3D point maps, complete camera poses, intrinsics, depth maps, and their corresponding confidence maps:

$$\mathcal{G}(\mathbf{I}, \mathbf{C}, \mathbf{D}) = (\hat{\mathbf{C}}_i, \hat{P}_i, \hat{D}_i, \hat{Y}_i)_{i=1}^N \quad (9)$$

The training objectives of OmniVGGT consist of three components: camera, depth, and point map.

$$\mathcal{L} = \mathcal{L}_{\text{camera}} + \mathcal{L}_{\text{depth}} + \mathcal{L}_{\text{pmap}}, \quad (10)$$

The camera loss $\mathcal{L}_{\text{camera}}$ supervises the cameras $\hat{\mathbf{g}}_i$ with ground truth \mathbf{g}_i using L1 loss:

$$\mathcal{L}_{\text{camera}} = \sum_{i=1}^N \|\hat{\mathbf{g}}_i - \mathbf{g}_i\|_1 \quad (11)$$

Following VGGT, we apply a confidence-aware regression loss to the depth and point map, both along with a gradient-based term:

$$\mathcal{L}_{\text{depth}} = \sum_{i=1}^N \left\| \Sigma_i^D \odot (\hat{D}_i - D_i) \right\| + \left\| \Sigma_i^D \odot (\nabla \hat{D}_i - \nabla D_i) \right\| - \alpha \log \Sigma_i^D \quad (12)$$

$$\mathcal{L}_{\text{pmap}} = \sum_{i=1}^N \left\| \Sigma_i^P \odot (\hat{P}_i - P_i) \right\| + \left\| \Sigma_i^P \odot (\nabla \hat{P}_i - \nabla P_i) \right\| - \alpha \log \Sigma_i^P \quad (13)$$

where \odot is the channel-broadcast element-wise product and α is a hyper-parameter. In addition, our depth D , point map P , and camera translations t in ground truths are all normalized by dividing the average Euclidean distance of all 3D points in the point map P to the origin. It should be noted that this normalization process is different from the normalization used in the information injection stage of OmniVGGT.

Frame Sampling Strategy. For every batch, we select between 2 and 24 frames from multiple random training scenes while maintaining a constant total of 24 frames within each batch. We sample each batch of images based on camera pose similarity. For each frame, all other frames are ranked according to their pose similarity, and the top N most similar frames are selected as its valid range. Then, for each sequence, we randomly choose one frame as the anchor frame and sample the remaining frames from its valid range. In addition, our depth D , point map P , and camera translations t in ground truths are all normalized by dividing the average Euclidean distance of all 3D points in the point map P to the origin. It should be noted that this normalization process is different from the normalization used in the information injection stage.

Training Details. We initialize OmniVGGT by using pre-trained weights from VGGT and fine-tune for 10 epochs of 12M iterations each. We train the model using the AdamW optimizer with a learning rate of 2×10^{-5} for prediction heads and 1×10^{-5} for backbone, which incorporates a 5K step linear warmup and cosine weight decay schedule. The p in our training objective is set to 10%. The spatial resolutions of the input images, depth maps, and point maps range from (518×168) to (518×518) . We also use ColorJitter as the data augmentation to enhance the model’s robustness in varying lighting conditions.

A.3. Baselines.

We mainly compare our approach with VGGT, Pow3R [22], and DUST3R [66]. Both Pow3R and DUST3R are feed-forward models that take a pair of views as input. The distinctive feature of Pow3R is that it can additionally incorporate camera intrinsics, poses, and depth maps as auxiliary inputs, but only in a pairwise input.

Table 8. **Training datasets statistic.** Each training epoch is composed of 20 datasets, and their relative quantities are reported as a ratio.

Index	Dataset	Scene Type	Real/Synthetic	Dynamic	# of Frames	Training Prob (%)
1	ARKitScene [6]	Indoor	Real	Static	1.2M	2.07
2	BlendedMVS [71]	Mixed	Real	Static	1.1M	2.07
3	DL3DV [33]	Mixed	Real	Static	21M	17.81
4	Dynamic Replica [23]	Indoor	Synthetic	Dynamic	2.8M	4.68
5	HyperSim [47]	Indoor	Synthetic	Static	70K	3.55
6	Kubric [16]	Object	Synthetic	Dynamic	1.3M	1.67
7	MapFree [3]	Outdoor	Real	Static	2.6M	9.03
8	MegaDepth [31]	Outdoor	Real	Static	1.2M	2.07
9	Matterport 3D [44]	Indoor	Real	Static	1.9M	3.48
10	MVS-Synth [21]	Outdoor	Synthetic	Static	12K	1.34
11	ScanNet [12]	Indoor	Real	Static	23M	4.75
12	ScanNet++ [72]	Indoor	Real	Static	7.8M	13.88
13	Spring [38]	Outdoor	Synthetic	Dynamic	4.9K	0.5
14	Tartanair [67]	Mixed	Synthetic	Static	3M	9.36
15	Uasol [7]	Outdoor	Real	Static	1.3M	2.41
16	Unreal 4K [58]	Outdoor	Synthetic	Static	16K	1.81
17	Vkitti [9]	Outdoor	Synthetic	Dynamic	42K	3.44
18	Waymo [56]	Outdoor	Real	Dynamic	7.9M	8.36
19	WildRGBD [68]	Object	Real	Static	1.9M	4.35

A.4. More Results of Auxiliary Information Guidance

In this subsection, we present the performance of auxiliary information guidance on additional datasets. Tables 9 and 10 report the results on ARKitScene [6] and OmniWorld (Game) [78], respectively. The methods have not been trained on these datasets.

A.5. Full Results of Multi-View Depth Estimation

In this subsection, we present the complete results of the multi-view depth evaluation in Section 5.2. For OmniVGGT, all images are resized to a fixed width of 518 pixels, and the aspect ratio is adjusted to the closest aspect ratio used during training according to the original images. The reported results are averaged over all samples. As shown in Table 11, we further analyze the impact of injecting different percentages of depth information. We observe that both VGGT and OmniVGGT show relatively poor Rel performance on the ScanNet dataset, mainly because the ground-truth depth in ScanNet is noisy (e.g., walls and floors are not smooth). Although the predicted depth maps are visually reasonable, the quantitative metrics appear degraded.

A.6. More Results of 3D Reconstruction

In this subsection, we present the complete 3D reconstruction results. Table 12 and 13 report the benchmark results on the 7-Scenes [53] and NRGB [4] datasets, respectively, including the effects of incorporating different types and percentages of auxiliary information.

A.7. More Visualizations

Fig. 7 presents a visual comparison between OmniVGGT and other methods on the 7-Scenes[53], NRGBD[54], and ETH3D [51] datasets. With the assistance of additional modality inputs (e.g., camera poses), OmniVGGT maintains accurate spatial relationships even in extreme cases—such as when two images have no overlap at all. Fig. 9 further demonstrates the strong generalization ability of OmniVGGT on in-the-wild data, where it achieves impressive results across both synthetic-engine-rendered and AI-generated images. Fig. 10 illustrates the reconstruction performance on image pairs that contain limited or no overlap between views. We also show the rollout examples of our method on the CALVIN benchmark in Fig. 11.

A.8. Architecture Ablation

In this subsection, we investigate the impact of different GeoAdapter strategies on model performance. We randomly select 100 batches from the Sintel [8] dataset, with 10 images per scene for inference, and evaluate the related metrics for depth and camera estimation. We trained the following three additional versions under the same training parameters and dataset. We experiment with three strategies: (a) *Replace*, where the original camera tokens are directly replaced by auxiliary camera tokens in each AA block, (b) *One-Layer Adapter*, where auxiliary camera tokens are only injected once before the AA blocks, and (c) *Depth ZeroConV*, where a ZeroConV layer is used for depth information injection. Table 14 reports the full results of our ablation experiments.

Table 9. **Impact of Auxiliary Information Injection on ARKitScenes (unseen)** [6]. We also show in green the absolute improvement w.r.t. the results without auxiliary information. The best results in each category are **bold**.

Method	Aux. information (%)		Depth		Camera		
	Depth	Camera	Abs Rel↓	$\delta < 1.25 \uparrow$	RRA@5°↑	RTA@ 5°↑	AUC@30° ↑
VGGT	✗	✗	0.048	98.90	72.17	35.94	60.52
OmniVGGT	✗	✗	0.035	99.02	73.66	50.03	65.82
OmniVGGT + aux. information	30	✗	0.035 (+0.000)	99.57 (+0.55)	77.53 (+3.87)	50.59 (+0.56)	67.92 (+2.10)
	50	✗	0.029 (+0.006)	99.52 (+0.50)	77.62 (+3.96)	51.97 (+1.94)	68.50 (+2.68)
	70	✗	0.021 (+0.014)	99.57 (+0.55)	76.34 (+2.68)	53.15 (+3.12)	68.25 (+2.43)
	100	✗	0.006 (+0.029)	99.97 (+0.95)	74.59 (+0.93)	53.69 (+3.66)	67.99 (+2.17)
	✗	30	0.035 (+0.000)	99.31 (+0.29)	77.60 (+3.94)	51.40 (+1.37)	68.46 (+2.64)
	✗	50	0.035 (+0.000)	99.30 (+0.28)	79.69 (+6.03)	53.92 (+3.89)	70.69 (+4.87)
	✗	70	0.034 (+0.001)	99.28 (+0.26)	84.69 (+11.03)	56.59 (+6.56)	74.21 (+8.39)
	✗	100	0.034 (+0.001)	99.89 (+0.87)	91.20 (+17.54)	64.98 (+14.95)	81.64 (+15.82)
	100	100	0.006 (+0.029)	99.97 (+0.95)	90.19 (+16.53)	67.00 (+16.97)	81.91 (+16.09)

Table 10. **Impact of Auxiliary Information Injection on OmniWorld-Game (unseen)** [78]. We also show in green the absolute improvement w.r.t. the results without auxiliary information. The best results in each category are **bold**.

Method	Aux. information (%)		Depth		Camera		
	Depth	Camera	Abs Rel↓	$\delta < 1.25 \uparrow$	RRA@5°↑	RTA@ 5°↑	AUC@30° ↑
VGGT [63]	✗	✗	0.260	79.10	73.97	58.57	63.75
OmniVGGT	✗	✗	0.240	80.50	74.20	59.39	63.86
OmniVGGT + aux. information	30	✗	0.208 (+0.032)	87.28 (+6.78)	74.42 (+0.22)	59.57 (+0.18)	63.91 (+0.05)
	50	✗	0.178 (+0.062)	90.68 (+10.18)	74.38 (+0.18)	59.48 (+0.09)	63.98 (+0.12)
	70	✗	0.151 (+0.089)	92.23 (+11.73)	74.63 (+0.43)	59.82 (+0.43)	64.20 (+0.34)
	100	✗	0.095 (+0.145)	94.54 (+14.04)	74.31 (+0.11)	60.54 (+1.15)	64.87 (+1.01)
	✗	30	0.239 (+0.001)	80.50 (+0.00)	74.29 (+0.09)	60.70 (+1.31)	64.75 (+0.89)
	✗	50	0.238 (+0.002)	80.51 (+0.01)	74.37 (+0.17)	61.93 (+2.54)	65.48 (+1.62)
	✗	70	0.237 (+0.003)	80.51 (+0.01)	74.42 (+0.22)	64.15 (+4.76)	68.06 (+4.20)
	✗	100	0.237 (+0.003)	80.52 (+0.02)	77.91 (+3.71)	65.46 (+6.07)	71.91 (+8.05)
	100	100	0.094 (+0.146)	94.57 (+14.07)	79.43 (+5.23)	68.89 (+9.50)	74.35 (+10.49)

In addition, Fig. 8 illustrates the feature maps of the spatial tokens and auxiliary depth tokens in OmniVGGT, with and without the use of the depth ZeroConV. We use Principal Component Analysis (PCA) to reduce the high-dimensional token embeddings to three dimensions and save them as RGB images. We observe that when the ZeroConv layer is applied to depth injection, the meaningful information within the auxiliary depth features (e.g., edges and background structures) is largely suppressed, causing the network to treat the injected depth as noise. In this case, the feature representations of OmniVGGT with and without auxiliary depth inputs remain nearly identical, and the resulting performance shows almost no difference. Therefore, we chose not to include the depth ZeroConV in our final network design.

Table 11. **Multi-view Depth Evaluation.** (Parentheses) denote training on data from the same domain. K”, “RT”, and “D” denote intrinsic, relative pose, and depth information, respectively. The best and second best results are **bold** and underlined respectively.

Method	GT	Extra	ScanNet [12]		ETH3D [51]		DTU [1]		T&T [26]		Average	
	range	info	rel↓	τ ↑	rel↓	τ ↑	rel↓	τ ↑	rel↓	τ ↑	rel↓	τ ↑
COLMAP [49, 50] (K+RT)	×	×	14.6	34.2	16.4	55.1	0.7	96.5	2.7	95.0	8.6	70.2
COLMAP Dense [49, 50] K+RT	×	×	38.0	22.5	89.8	23.2	20.8	69.3	25.7	76.4	43.6	47.9
MVSNet [70] (K+RT)	✓	×	22.7	20.9	21.6	35.6	(1.8)	(86.7)	6.5	74.6	12.3	11.1
Vis-MVSNet [74] (K+RT)	✓	×	8.9	33.5	10.8	43.3	1.8	87.4	4.1	7.2	6.4	42.9
MVS-Former++ (K+RT)	✓	×	15.2	21.9	21.4	32.5	(1.2)	(91.9)	7.6	71.5	10.8	8.5
CER-MVS [11] (K+RT)	×	×	21.1	24.3	11.7	47.5	4.1	71.3	6.4	82.1	10.8	56.3
DUST3R [66]	×	med	(3.1)	(71.8)	3.0	76.0	3.9	68.6	3.3	75.1	3.3	72.9
Pow3R [22]	×	med	(3.2)	(68.8)	3.0	74.7	3.0	74.3	3.3	76.6	3.1	73.6
VGGT [63]	×	med	(3.7)	(70.0)	1.7	87.2	0.9	95.4	1.7	90.6	2.0	85.8
OmniVGGT	×	med	(3.6)	(72.3)	1.8	87.5	1.1	93.9	1.8	90.0	2.1	85.9
Pow3R [22] w/ 100% (K+RT)	×	med	(3.1)	(71.4)	2.8	77.1	1.5	91.1	3.2	78.2	2.7	79.5
OmniVGGT w/ 100% (K+RT)	×	med	(3.7)	(72.2)	1.8	87.8	1.2	93.6	1.8	89.9	2.1	85.9
OmniVGGT w/ 30% D	×	med	(2.3)	(85.5)	0.7	97.9	0.5	99.2	1.2	93.2	1.2	94.0
OmniVGGT w/ 50% D	×	med	(2.3)	(85.9)	0.6	98.6	0.4	99.4	1.0	94.4	1.1	94.6
OmniVGGT w/ 70% D	×	med	(2.3)	(86.0)	0.6	98.7	0.4	99.4	0.9	95.5	1.1	<u>94.9</u>
OmniVGGT w/ 100% D	×	med	(<u>2.3</u>)	(85.6)	<u>0.5</u>	<u>98.7</u>	<u>0.3</u>	99.5	<u>0.9</u>	<u>95.5</u>	<u>1.0</u>	94.8
OmniVGGT w/ 100% (K+RT+D)	×	med	(2.2)	(86.7)	0.5	98.7	0.3	<u>99.4</u>	0.9	95.6	1.0	95.1

Table 12. **3D reconstruction on the 7-scenes [53] datasets.** K”, “RT”, and “D” denote intrinsic, relative pose, and depth information, respectively. The best and second best results in each category are **bold** and underlined respectively.

Method	Acc↓		Comp↓		NC↑	
	Mean	Med.	Mean	Med.	Mean	Med.
VGGT [63]	0.087	0.039	0.091	0.039	0.787	0.890
Fast3R [69]	0.164	0.108	0.163	0.080	0.686	0.775
DUST3R-GA [66]	0.146	0.077	0.181	0.067	0.736	0.839
MAS3R-GA [29]	0.185	0.081	0.180	0.069	0.701	0.792
MonST3R-GA [75]	0.248	0.185	0.266	0.167	0.672	0.759
Spann3R [60]	0.298	0.226	0.205	0.112	0.650	0.730
SLAM3R [34]	0.287	0.155	0.226	0.066	0.644	0.720
CUT3R [65]	0.126	0.047	0.154	0.031	0.727	0.834
OmniVGGT	0.104	0.037	<u>0.112</u>	0.031	<u>0.763</u>	<u>0.875</u>
OmniVGGT w/ 30% D	0.098	0.034	0.110	0.028	0.778	0.889
OmniVGGT w/ 50% D	0.103	0.033	0.106	0.028	0.781	0.890
OmniVGGT w/ 70% D	0.094	0.045	0.094	0.033	0.785	0.885
OmniVGGT w/ 100% D	0.085	0.034	0.085	0.027	<u>0.789</u>	<u>0.894</u>
OmniVGGT w/ 30% (K+RT)	0.100	0.034	0.107	0.027	0.761	0.875
OmniVGGT w/ 50% (K+RT)	0.101	0.035	0.108	0.027	0.761	0.875
OmniVGGT w/ 70% (K+RT)	0.089	0.022	0.096	0.022	0.771	0.886
OmniVGGT w/ 100% (K+RT)	<u>0.037</u>	<u>0.017</u>	<u>0.049</u>	<u>0.019</u>	0.778	0.893
OmniVGGT w/ 100% (K+RT+D)	0.036	0.017	0.036	0.017	0.810	0.912

Table 13. **3D reconstruction on the NRGB [4] datasets.** K”, “RT”, and “D” denote intrinsic, relative pose, and depth information, respectively. The best and second best results in each category are **bold** and underlined respectively.

Method	Acc↓		Comp↓		NC↑	
	Mean	Med.	Mean	Med.	Mean	Med.
VGGT [63]	0.087	0.039	0.091	0.039	0.787	0.890
Fast3R [69]	0.164	0.108	0.163	0.080	0.686	0.775
DUST3R-GA [66]	0.146	0.077	0.181	0.067	0.736	0.839
MAS3R-GA [29]	0.185	0.081	0.180	0.069	0.701	0.792
MonST3R-GA [75]	0.248	0.185	0.266	0.167	0.672	0.759
Spann3R [60]	0.298	0.226	0.205	0.112	0.650	0.730
SLAM3R [34]	0.287	0.155	0.226	0.066	0.644	0.720
CUT3R [65]	0.126	0.047	0.154	0.031	0.727	0.834
OmniVGGT	0.104	0.037	<u>0.112</u>	0.031	<u>0.763</u>	<u>0.875</u>
OmniVGGT w/ 30% D	0.098	0.034	0.110	0.028	0.778	0.889
OmniVGGT w/ 50% D	0.103	0.033	0.106	0.028	0.781	0.890
OmniVGGT w/ 70% D	0.094	0.045	0.094	0.033	0.785	0.885
OmniVGGT w/ 100% D	0.085	0.034	0.085	0.027	<u>0.789</u>	<u>0.894</u>
OmniVGGT w/ 30% (K+RT)	0.100	0.034	0.107	0.027	0.761	0.875
OmniVGGT w/ 50% (K+RT)	0.101	0.035	0.108	0.027	0.761	0.875
OmniVGGT w/ 70% (K+RT)	0.089	0.022	0.096	0.022	0.771	0.886
OmniVGGT w/ 100% (K+RT)	<u>0.037</u>	<u>0.017</u>	<u>0.049</u>	<u>0.019</u>	0.778	0.893
OmniVGGT w/ 100% (K+RT+D)	0.036	0.017	0.036	0.017	0.810	0.912

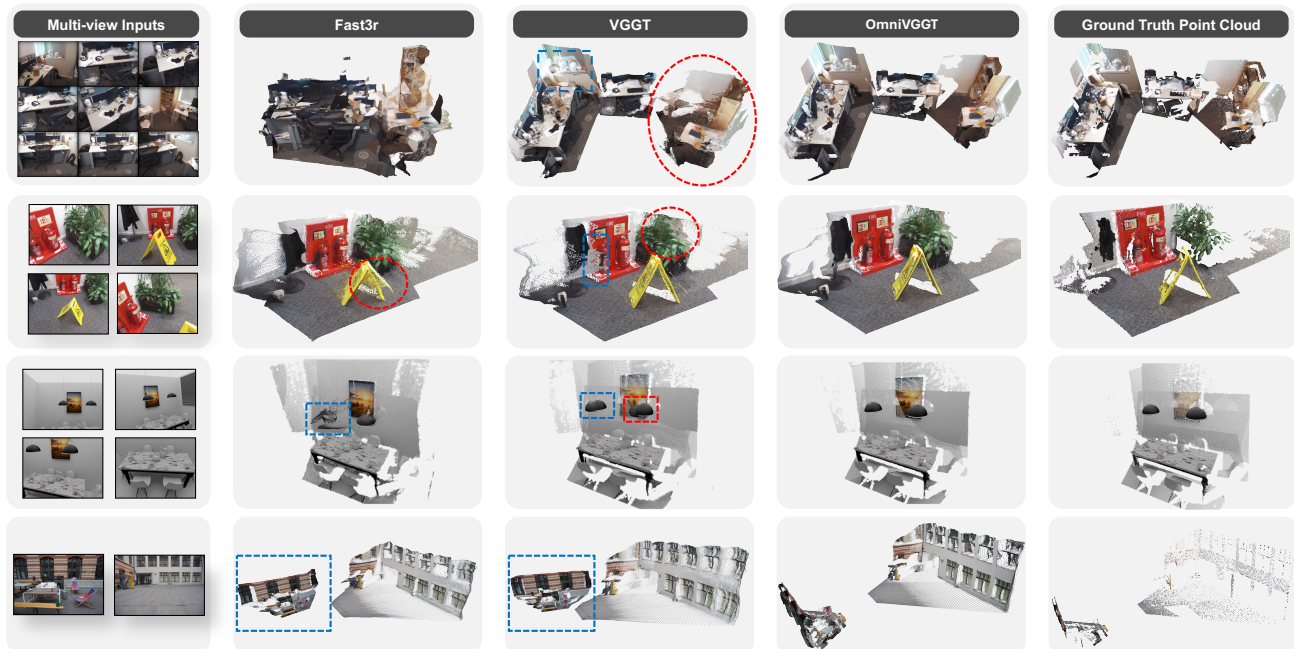


Figure 7. Visual Comparisons on 7-Scenes [53], NRGBD [4], and ETH3D [51] datasets.

Table 14. Ablation of GeoAdapter architectures. We compare different GeoAdapter designs on the Sintel [8] dataset. The ‘Replace’ refers to directly substituting the original camera tokens with auxiliary camera tokens, whereas ‘One-Layer GeoAdapter’ represents injecting auxiliary camera tokens only once before the encoder. ‘Depth ZeroConV’ denotes using ZeroConV for depth injection.

Architecture	Depth		Camera		
	Abs Rel \downarrow	$\delta < 1.25 \uparrow$	RRA@5 $^\circ \uparrow$	RTA@5 $^\circ \uparrow$	AUC@30 $^\circ \uparrow$
<i>w/o (K+RT+D) Auxiliary Information</i>					
(a) Replace	0.845	64.74	93.40	30.88	64.74
(b) One-Layer Adapter	0.604	68.74	96.78	44.92	68.74
(c) Depth ZeroConV	0.569	70.71	96.44	51.86	69.70
(d) OmniVGGT	0.558	71.46	96.15	54.01	70.83
<i>w/ (K+RT) Auxiliary Information</i>					
(a) Replace	0.842	65.11	96.98	55.66	76.28
(b) One-Layer Adapter	0.563	70.16	97.54	58.84	77.00
(c) Depth ZeroConV	0.569	70.71	99.65	69.29	83.18
(d) OmniVGGT	0.553	72.36	99.97	75.83	85.35
<i>w/ Depth Auxiliary Information</i>					
(a) Replace	0.670	82.96	94.69	52.04	71.61
(b) One-Layer Adapter	0.107	85.91	95.97	52.34	74.66
(c) Depth ZeroConV	0.570	71.02	95.45	56.10	72.93
(d) OmniVGGT	0.106	85.95	96.93	59.73	77.16
<i>w/ (K+RT+D) Auxiliary Information</i>					
(a) Replace	0.655	82.96	97.08	57.61	77.83
(b) One-Layer Adapter	0.133	85.65	99.97	60.89	81.66
(c) Depth ZeroConV	0.505	71.11	99.72	71.66	84.12
(d) OmniVGGT	0.106	85.95	99.97	76.33	85.99

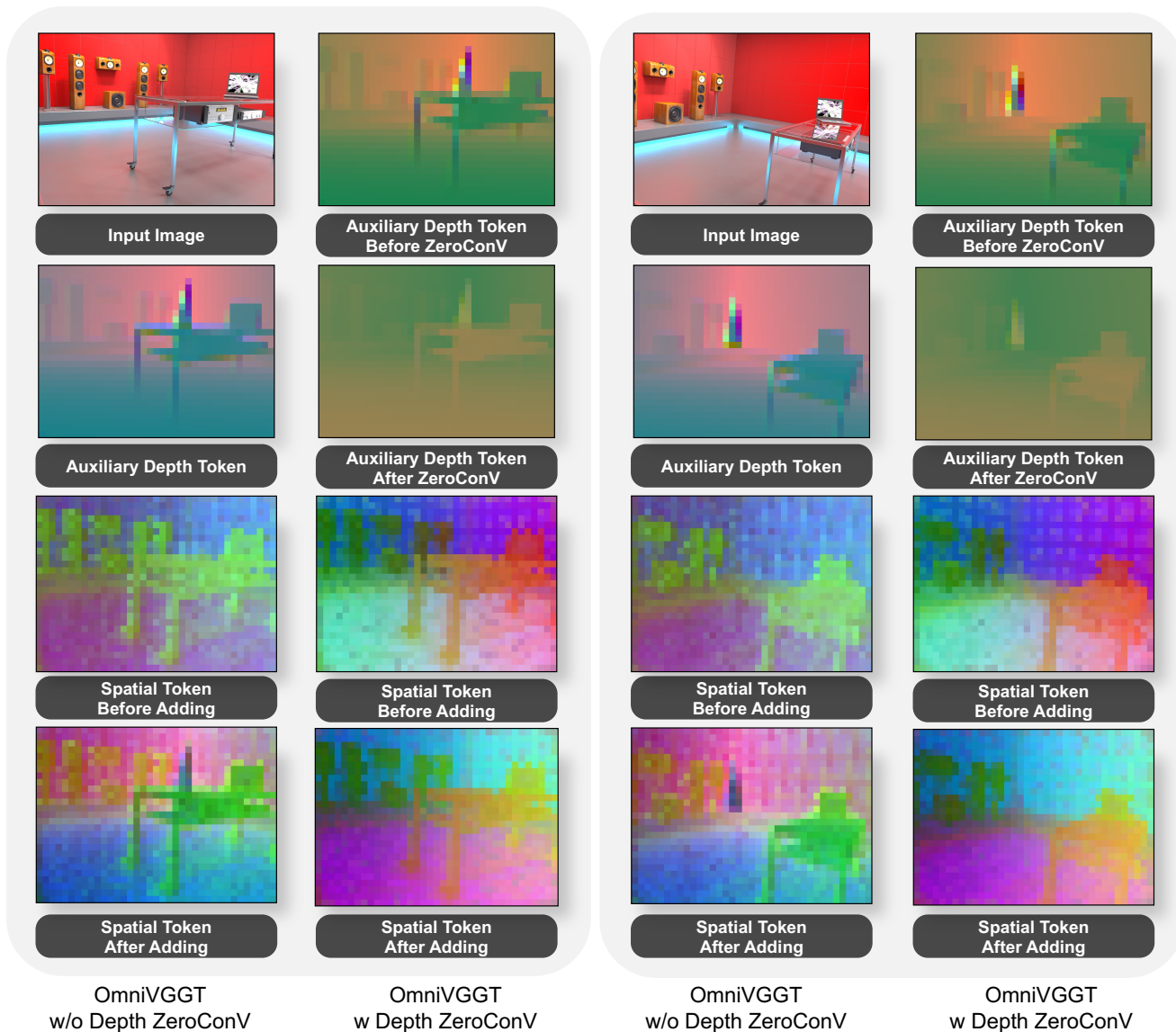


Figure 8. **Feature Map Visualization Comparison Between OmniVGGT and OmniVGGT w/ Depth ZeroConV.** **Left Column:** OmniVGGT without applying the ZeroConV to the depth adapter. From top to bottom: the input image, the feature map of the auxiliary depth token after passing through the depth encoder; the spatial token feature map obtained from the image after the DINO encoder; and the spatial token feature map after adding the auxiliary depth tokens. **Right Column:** OmniVGGT with the ZeroConV applied to the auxiliary depth information. From top to bottom: the auxiliary depth token feature map before and after the ZeroConV; and the spatial token feature maps before and after the addition of auxiliary depth tokens.



Figure 9. Feed-Forward 3D Point Map by OmniVGGT with In-The-Wild Inputs.

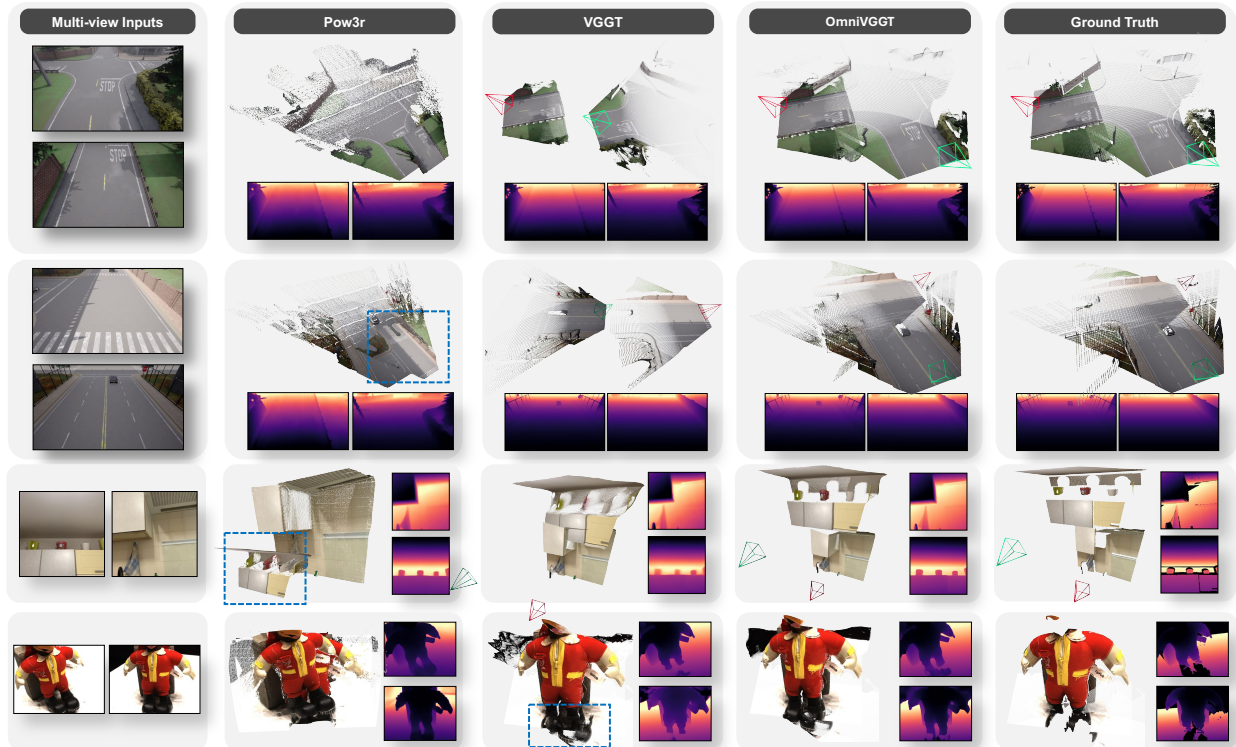


Figure 10. More Visualizations on Image Pairs Input.

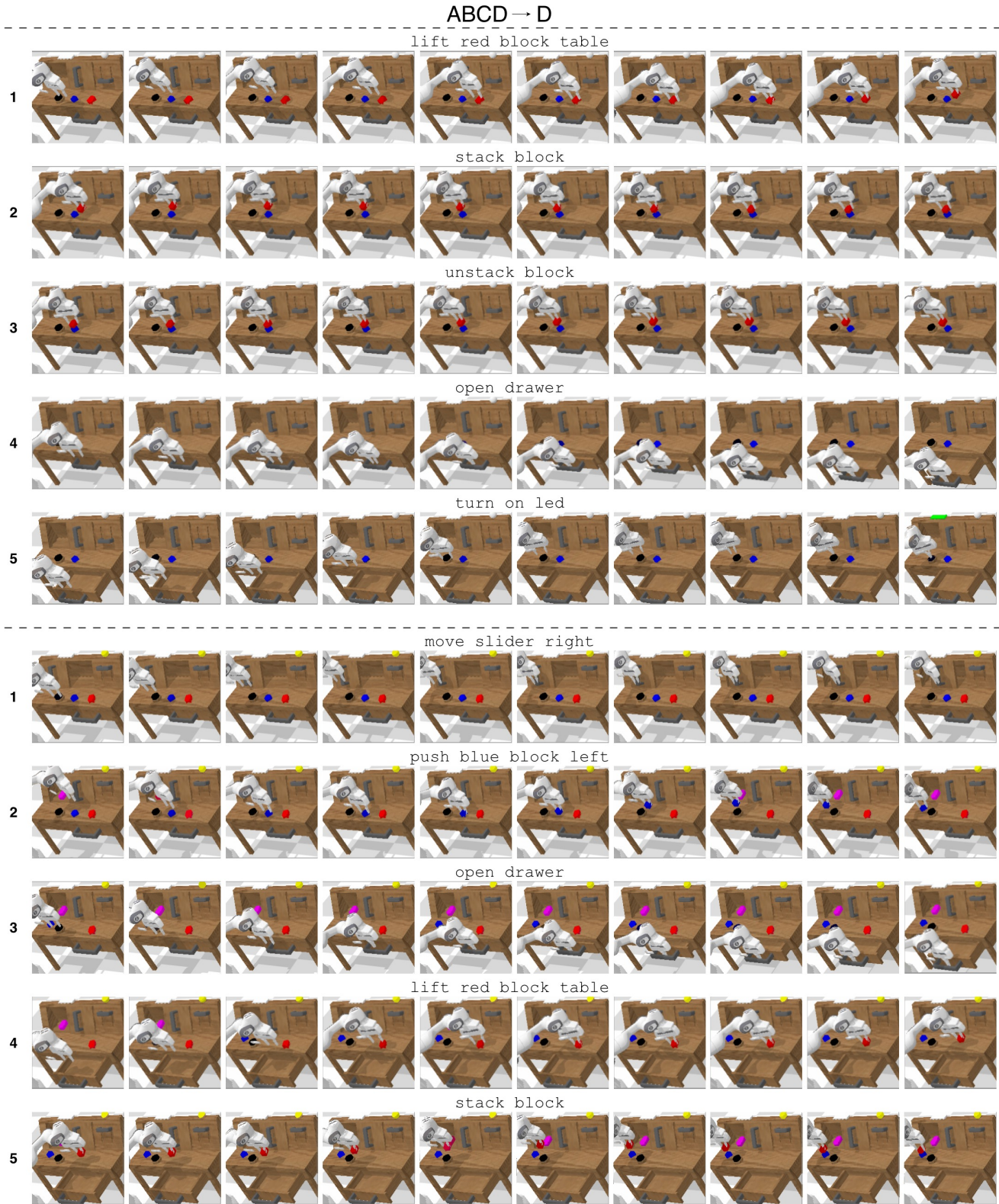


Figure 11. Ours Rollouts on the ABCD→D split of the CALVIN benchmark.